iScience

CellPress
OPEN ACCESS

Article

Hydrogel with ROS scavenging effect encapsulates BR@Zn-BTB nanoparticles for accelerating diabetic mice wound healing via multimodal therapy

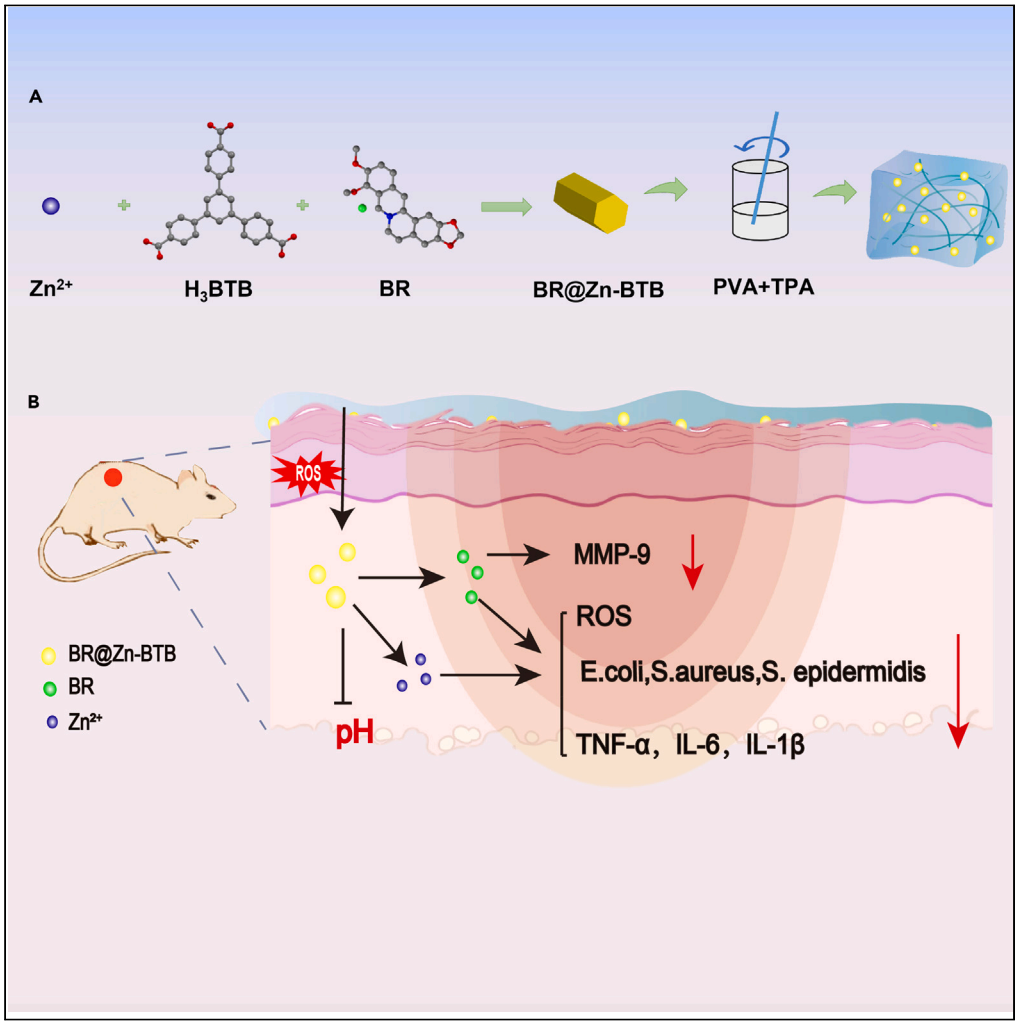

Jing-Jing Hu, Xue-Zhao Yu, Shu-Qin Zhang, ..., Wen-Hua Zhang, Jin-Xiang Chen, Qun Zhang

jxchen@smu.edu.cn (J.-X.C.)
zq1979@smu.edu.cn (Q.Z.)

Highlights

A hydrogel-dressing nanoparticle of BR@Zn-BTB/Gel has been constructed

The nanoparticle disintegrates slowly in the diabetic wound microenvironment

The nanoparticle has excellent multifunctional properties

The nanoparticle synergistically promotes diabetic wound healing

Hu et al., iScience 26, 106775
June 16, 2023 © 2023
https://doi.org/10.1016/j.isci.2023.106775

iScience

CellPress
OPEN ACCESS

Article

Hydrogel with ROS scavenging effect encapsulates BR@Zn-BTB nanoparticles for accelerating diabetic mice wound healing via multimodal therapy

Jing-Jing Hu,[1,4] Xue-Zhao Yu,[1,4] Shu-Qin Zhang,[1] Yu-Xuan Zhang,[2] Xiao-Lin Chen,[1] Zhu-Jun Long,[1] Hua-Zhong Hu,[1] Deng-Hui Xie,[1] Wen-Hua Zhang,[3] Jin-Xiang Chen,[2,*] and Qun Zhang[1,5,*]

SUMMARY

The strategies for eliminating excess reactive oxygen species (ROS) or suppressing inflammatory responses on the wound bed have proven effective for diabetic wound healing. In this work, a zinc-based nanoscale metal-organic framework (NMOF) functions as a carrier to deliver natural product berberine (BR) to form BR@Zn-BTB nanoparticles, which was, in turn, further encapsulated by hydrogel with ROS scavenging ability to yield a composite system of BR@Zn-BTB/Gel (denoted as BZ-Gel). The results show that BZ-Gel exhibited the controlled release of Zn^{2+} and BR in simulated physiological media to efficiently eliminated ROS and inhibited inflammation and resulted in a promising antibacterial effect. *In vivo* experiments further proved that BZ-Gel significantly inhibited the inflammatory response and enhanced collagen deposition, as well as to re-epithelialize the skin wound to ultimately promote wound healing in diabetic mice. Our results indicate that the ROS-responsive hydrogel coupled with BR@Zn-BTB synergistically promotes diabetic wound healing.

INTRODUCTION

Diabetic chronic wounds are one of the most common and serious complications of diabetic patients and have become a growing problem worldwide.[1] Due to the limited regenerative capacity after injury, diabetic wounds, especially diabetic foot ulcers (DFU) would be deteriorated and seriously threatened the health and life of patients, resulting in the 5-year survival rate being only 29–50%.[2,3] The increased DFU-related amputations and medical expenditures have become a heavy burden on the public health system and patients.[4] At present, hyperbaric oxygen therapy and skin replacement therapy are the main treatment methods for DFU-related diabetic wounds.[5] But there are some disadvantages, such as poor therapeutic efficacy and high treatment cost. Although some treatments are effective for selective patients, diabetic wounds are in general difficult to cure.[6]

Diabetic wounds are chronic and incurable mainly due to a variety of cytokine metabolism disorders and impaired procedural repair.[7,8] At present, its detailed pathogenesis is not yet clear but is found to relate to vascular disease, neuropathy, pathogen infection, oxidative stress, chronic inflammation, extracellular matrix (ECM) abnormalities, etc.[9] Among the physiological and pathological factors that cause this symptom, the continuous inflammatory response and excessive reactive oxygen species (ROS) in the wounds are two key reasons.[10,11] Due to impaired glucose metabolism, excessive ROS and inflammatory factors produced by macrophages cannot be removed normally in the acute inflammation stage of diabetes (or the mid-stage of wound healing), leading to cytotoxicity and skin tissue damage.[12] In addition, excessive ROS and chronic inflammation also up-regulate the expression of the zinc-dependent matrix metalloproteinases-9 (MMP-9) by activating the nuclear factor-kappa B (NF-κB) pathway,[13] which disrupt the balance of ECM deposition and remodeling and prevent epithelial closure.

Excessive activation of MMP-9 can lead to the destruction of local ECM. Without the scaffold provided by ECM, cell migration will be impaired and the epithelial closure of the wound will be blocked. This increases the risk of infection.[14,15] Once bacterial infection commenced, it aggravates the inflammatory response and duration, which, in turn, further promotes the expression of MMP-9 and results in a vicious circle leading to prolonged wound healing.[16] Thus, the balance between MMP-9 and metalloproteinase inhibitor-1 (TIMP-1)

[1]Office of Clinical Trial of Drug, Guangdong Provincial Key Laboratory of Bone and Joint Degeneration Diseases, The Third Affiliated Hospital of Southern Medical University, Guangzhou 510663, China

[2]NMPA Key Laboratory for Research and Evaluation of Drug Metabolism, Guangdong Provincial Key Laboratory of New Drug Screening, School of Pharmaceutical Sciences, Southern Medical University, Guangzhou 510515, People's Republic of China

[3]College of Chemistry, Chemical Engineering and Materials Science, Soochow University, Suzhou 215123, People's Republic of China

[4]These authors contributed equally

[5]Lead contact

*Correspondence: jxchen@smu.edu.cn (J.-X.C.), zq1979@smu.edu.cn (Q.Z.)

https://doi.org/10.1016/j.isci.2023.106775

is a key determinant of the accumulation and remodeling of collagen and non-collagen ECM components in the later stage of wound healing.[17]

Contemporary efforts have focused on the mechanism of ROS elimination, angiogenesis promotion, local anti-inflammatory, and anti-infection using a large number of innovative composite materials, such as nanoparticles, electrospun fibers, and composite hydrogels. These genuinely designed materials also showed great potential in accelerating wound healing. For example, the constructed inorganic nano-enzymes could efficiently remove excess ROS produced by wounds.[18] The angiogenesis-promoting drugs delivered by a carrier could promote the formation of blood vessels in diabetic wounds.[19] The super-porous hydrogel dressing with silver-ethylene interaction could inhibit bacterial infection and promote wound healing.[20] Nevertheless, for the complicated microenvironment of diabetic wounds, treatment regimens based on a single mechanism often fail to provide an ideal therapeutic outcome, and multifunctional wound care strategies are urgently needed to deal with difficult-to-heal diabetic wounds.

Berberine (BR) is a naturally occurring isoquinoline alkaloid with multiple functions such as anti-oxidation, antibacterial, and anti-inflammatory. It has attracted widespread attention in the treatment of various diseases.[21] Previous studies have shown that BR can reduce the expression of pro-inflammatory cytokines (such as IL-6, TNF-α, etc.). Recently, a series of studies have shown that BR has a beneficial effect on the treatment of wound healing and endothelial injury.[22] In addition, BR is a broad-spectrum plant antibiotic with excellent antibacterial activity and has the potential to act as an antibacterial therapeutic agent.[23] However, due to its relatively poor solubility in plasma, low biological stability, and limited bioavailability, BR has not been widely adopted clinically.[24] Therefore, maintaining a safe concentration of BR in local wounds and improving its bioavailability are important prerequisites for the use of BR to treat diabetic wounds.

Nanoscale metal-organic frameworks (NMOFs) are considered ideal drug carriers for potential biomedical applications due to their high porosity and the biological utility of both ligands and central ions.[25–27] In particular, some NMOFs can operate synergistically with loaded drugs, thereby greatly improving the treatment efficacy.[28] For example, PCN-224 and HKUST-1 have photothermal and photoelectronic conversion capabilities, which showed great potential in eliminating bacterial infections in wounds.[29–31]

The central metal ions can be released during the degradation of NMOFs.[32] In this sense, choosing a suitable metal ion for an NMOF can increase the drug loading rate while creating a favorable ionic microenvironment for promoting wound healing. Previous studies have shown that the presence of Zn^{2+} can significantly increase the activity of Cu, Zn-superoxide dismutase (CuZn SOD) to promote skin cells to fight against ROS,[33] as well as to inhibit bacterial reproduction by destroying the stability of bacterial capsules.[34]

Polyvinyl alcohol (PVA)-based hydrogel has become an ideal wound dressing due to its good hydrophilicity, biocompatibility, and adjustable mechanical properties.[35] Taking into account the excessive ROS level in diabetic wounds, the ROS-responsive linking agent N,N,N′,N′-tetramethyl-1,3-propanediamine, 4-(bromomethyl) phenylboronic acid (TPA) and PVA was used to cross-link and polymerize to prepare a composite hydrogel TPA-PVA, which showed antibacterial and ROS scavenging properties due to the introduction of quaternary ammonium and phenyl borate functionalities.[36,37] Studies have shown that composite dressings prepared by encapsulating drugs or nanomaterials with hydrogels lead to the improvement of the curative effect while avoiding adverse inflammatory reactions caused by particles. We expect that a sustained release of Zn^{2+} and BR from the composite hydrogel dressing and the ROS-responsive disintegration of the scaffold will jointly build a favorable microenvironment for promoting diabetic wound healing.

Herein, the assembly of carboxylic acid ligand 1,3,5-tris(4-carboxyphenyl) benzene (H_3BTB) and Zn^{2+} afforded NMOF Zn-BTB as a drug carrier for BR encapsulation. As far as we are aware, there are no previous reports on the use of Zn-BTB NMOF as the drug carrier presumably due to the general water sensitivity of Zn-based MOFs. The BR-loaded Zn-BTB is then embedded in the hydrogel scaffold of TPA-PVA to obtain the composite BR@Zn-BTB/Gel (abbreviated as BZ-Gel). The hydrogel composite dressing removes ROS

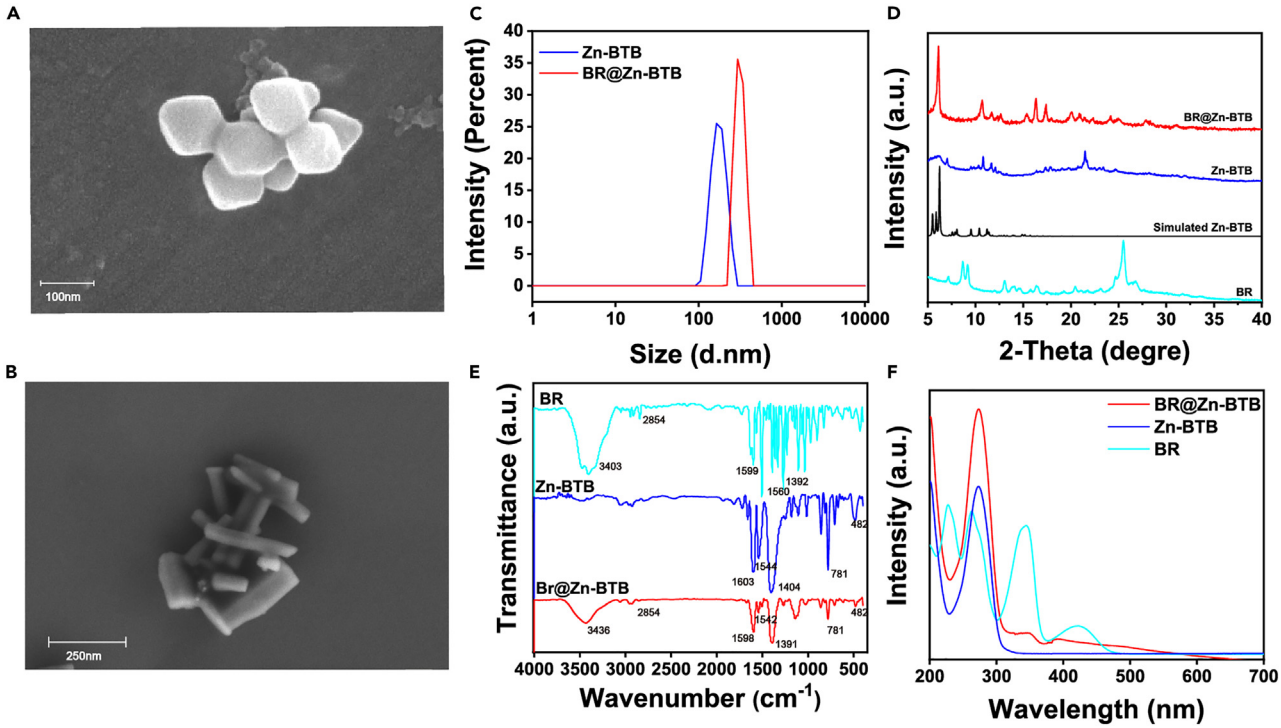

Figure 1. Characterization of Zn-BTB and BR@Zn-BTB particles

(A and B) The SEM images of (A) Zn-BTB and (B) BR@Zn-BTB.

(C) The particle size distribution of Zn-BTB and BR@Zn-BTB by DLS.

(D) The PXRD spectra of the BR, simulated Zn-BTB, experimental Zn-BTB, and BR@Zn-BTB.

(E) The FT-IR spectra of BR, Zn-BTB, and BR@Zn-BTB.

(F) The UV-Vis spectra of the BR, Zn-BTB, and BR@Zn-BTB.

from wounds and slowly degrades, accompanied by the release of Zn^{2+} and BR. With the sustained release, the safety and stability of BR are guaranteed.

Critically, the prepared stent has excellent anti-inflammatory, antibacterial, and antioxidant properties to synergistically promote diabetic wound healing. This study reveals the promising potential of ROS scavenging hydrogel scaffolds in combination with BR@Zn-BTB NMOF for the treatment of diabetic wounds in a multi-purposeful manner.

RESULTS AND DISCUSSION

Preparation and characterization of BR@Zn-BTB particles and BZ-Gel hydrogel scaffold

In this work, the BR@Zn-BTB nanoparticles were prepared by a facile one-pot synthetic method, the specific condition exploration process was shown in Figure S1. The drug loading efficiency of BR of about 35% was detected by the standard curve method as shown in Figure S2. As indicated by SEM (Figures 1A and 1B), the as-synthesized Zn-BTB appeared amorphous while BR@Zn-BTB presented as a columnar shape with clear and neat edges. The difference in the morphology of the two nanoparticles may be due to the introduction of BR which changed the coordination environment of metal ions and ligands. It was reported that the MOFs constructed by the same metal ion and ligand has morphology change due to slight changes in the synthetic conditions.[38] As shown in Figure 1C, the average particle sizes of the prepared Zn-BTB and BR@Zn-BTB were approximately 150 $\pm$ 0.37 nm and 250 $\pm$ 0.52 nm, respectively, which were consistent with their SEM results. As shown in the PXRD spectra (Figure 1D), the prepared Zn-BTB and BR@Zn-BTB had characteristic diffraction peaks at 2θ angles of 6.24°, 7.58°, and 11.2°, indicating that BR@Zn-BTB maintains the Zn-BTB structure with high crystallinity. The slight change in the diffraction pattern of the BR@Zn-BTB should be attributed to the BR molecules retained in the Zn-BTB pores.[39] The IR spectrum analysis was shown in Figure 1E, two intense bands at 1544 cm^{-1} and 1404 cm^{-1} were observed in Zn-BTB, which were assigned to the asymmetric and symmetric stretching vibrations of $\nu_{C=O}$ of carboxylate groups. The peak

that appeared at 2844 cm^{-1} revealed the existence of a -OMe group and thus the presence of BR. Both the absorption peaks of carboxylate in Zn-BTB and -OMe group in BR were retained in the BR@Zn-BTB spectrum. The UV-Vis analysis further confirmed that BR was successfully loaded into Zn-BTB (Figure 1F). The characteristic absorption peak of Zn-BTB was observed at 271 nm, and the strong absorption band of BR appeared at 346 nm. These two characteristic peaks were also inherited in the BR@Zn-BTB. These results collectively indicate that BR@Zn-BTB contains both BR and Zn-BTB.

As water-based soft material, the hydrogel can absorb wound exudate to prevent the wound from drying out and isolate the wound from the environment. It is an ideal choice for promoting wound healing. In previous studies, hydrogels were used as carriers for sustained drug release without other notable functions. Since diabetic wounds are generally in a state of excessive oxidative stress, a hydrogel with the function of ROS scavenging was synthesized as a nanoparticle carrier in this work. First, N,N,N′,N′-tetramethyl-1,3-propanediamine and 4-(bromomethyl)phenylboronic acid are used to synthesize ROS-responsive linker TPA, and the structure of TPA was determined by ^{1}H NMR (Figure S3). The ROS-responsive hydrogel crosslinked quickly by simply mixing PVA and TPA through the reactions between phenylboronic acid in TPA and alcohol hydroxyl groups in PVA. As shown in Figure 2A, TPA and PVA were liquid, and when they were mixed, a solid colloid with a certain viscosity is formed. Subsequently, the ROS-responsive degradation behavior of hydrogel was evaluated in PBS with the introduction of hydrogen peroxide (H_2O_2). It was observed from Figure 2B that the hydrogel degraded within 2 h in PBS containing H_2O_2. In contrast, the hydrogel remained stable in PBS in the absence of H_2O_2, indicating that the hydrogel responds to ROS causing its degradation. Meanwhile, the ROS-scavenging ability of the hydrogel was studied using the HRP-TMB method. HRP could catalyze the decomposition of H_2O_2 to generate hydroxyl radicals (·OH). These ·OH then reacted with TMB to produce a blue azo compound, which has UV-Vis absorption peaks at 650 nm.[40] As shown in Figure 2C, the peak of the characteristic absorption peaks at 650 nm gradually decreased within 2 h, indicating that the concentration of residual H_2O_2 in the solution was decreasing. Also, the color of the solution gradually faded, indicating that this hydrogel could gradually quench the generated ROS. After the determination of the ROS-scavenging ability of the hydrogel, the as-synthesized BR@Zn-BTB was evenly loaded, and the state of the composite BZ-Gel could be observed in Figure 2D. It can be seen that BZ-Gel has good adhesion and tensile properties. The internal structure was further observed by SEM. As shown in Figure 2E, the pure hydrogel had relatively uniform pores with a pore size of about 4 μm. The composite hydrogels Z-Gel and BZ-Gel loaded with nanoparticles had significantly larger pores than pure hydrogels, with the BZ-Gel having the largest pore size of around 8 μm. It should be noted that macro-porous hydrogels facilitated cell proliferation and migration compared to non-macro-porous hydrogels.[41]

Cumulative release of BR and Zn^{2+} in BR@Zn-BTB and BZ-Gel hydrogel scaffold

BR@Zn-BTB was placed in PBS at pH values of 6.5, 7.0, 7.4, and 8.0 to evaluate its release characteristics at different pH.[42] As shown in Figure 3A, as the pH value increases, the release rate of BR from BR@Zn-BTB gradually increases. Specifically, the release rate of BR from BR@Zn-BTB at 36 h is close to 80% at pH 8.0, 60% at pH 7.4, and 40% at both pH 7.0 and 6.5. At the same time, we measured the release rate of Zn^{2+} from BZ-Gel at different pH (Figure S4). The supplement also proves that the release of Zn^{2+} is faster at higher pH. Since the surface of normal skin is usually weakly acidic with a pH value in-between 4–6. In chronic and infected wounds, the pH changes to alkaline, usually in-between 7.5–8.9.[43] Therefore, it can be inferred that BR@Zn-BTB is suitable for the treatment of malignant diabetic foot wounds.

The release behaviors of BR and Zn^{2+} in BZ-Gel were compared and evaluated in a release medium of physiological pH 7.4. As shown in Figure 3B, the BR released from BZ-Gel was sustained and significantly delayed within 36 h as compared to BR@Zn-BTB. It is closely related to the instability of Zn-BTB directly exposed to PBS. Most importantly, the release time of BR in BZ-Gel can reach 100 h and above, and the release rate is relatively slow, indicating that the slow disintegration of the hydrogel ensures the sustained release of the drug to avoid the toxicity of BR caused by burst release. As shown in Figure 3C, the Zn^{2+} released from the BZ-Gel is also significantly prolonged (only 19.8% Zn^{2+} in the first 36 h) compared with BR@Zn-BTB (approximately 38.9% within 36 h). In the subsequent release process, the release rate remains stable and slow, which may play an important role in the wound healing process. The above results showed that the hydrogel further released BR and zinc ions slowly. The above results indicated that the release of BR and Zn^{2+} in the hydrogel was further sustained.

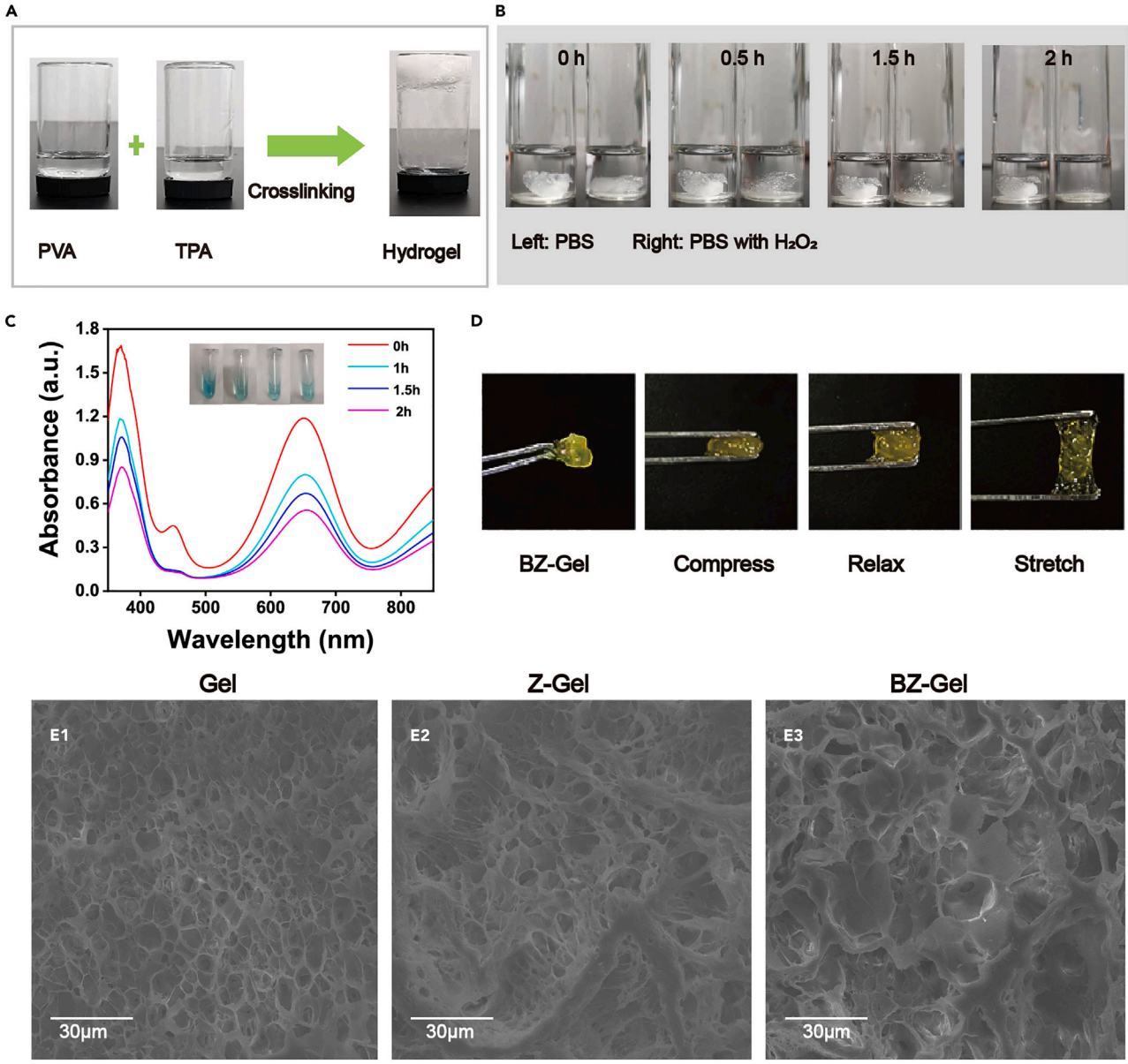

Figure 2. The synthesis and characteristics of hydrogels

(A) Photographs of the solution to hydrogel transition by mixing PVA solution and TPA solution.

(B) Photographs of the hydrogel degradation in H_2O_2.

(C) The UV-Vis spectra of TMB + H_2O_2 remaining (Initial concentration of H_2O_2: 100 mM).

(D) Photographs of the adhesion behavior of BZ-Gel.

(E) Representative SEM images of the Gel (E1), Z-Gel (E2), and BZ-Gel (E3) (scar bar: 30 μm).

In *vitro* antibacterial activity of BZ-Gel hydrogel scaffold

The inhibitory effect of BZ-Gel on *Staphylococcus aureus*, *Staphylococcus epidermidis*, and *Escherichia coli* was measured by the disc diffusion method.[20] As shown in Figure 4A, for *S. aureus*, the Gel, Z-Gel, B-Gel, and BZ-Gel groups all showed inhibition zones, and the inhibition zones in the BZ-Gel group were larger than other groups. For *S. epidermidis*, it was observed that the bacteriostatic zone around BZ-Gel was greater than that of Z-Gel and B-Gel groups, while the zone of inhibition in the pure Gel group was not obvious. In contrast, for *E. coli*, the inhibition zones in Gel, Z-Gel, B-Gel, and BZ-Gel groups had no obvious difference. The diameter of the inhibition zone was shown in Figure 4B, for gram-positive bacteria

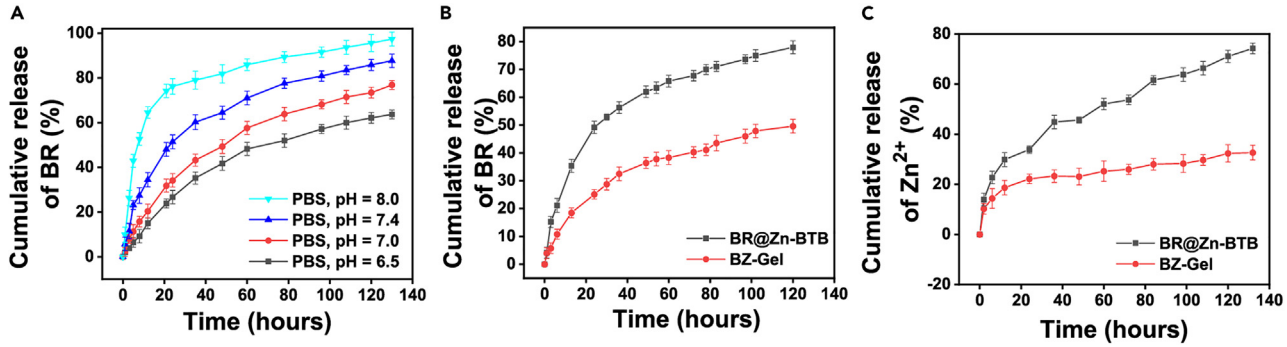

Figure 3. The slow-release characteristics of BZ-Gel

(A) BR released from BR@Zn-BTB in PBS with different pH values.

(B) BR released from BR@Zn-BTB and BZ-Gel at physiological pH (pH = 7.4).

(C) Zn^{2+} released from BR@Zn-BTB and BZ-Gel at physiological pH (pH = 7.4).

(*S. aureus* and *S. epidermidis*), the inhibition zone diameters of the Z-Gel and B-Gel groups were equivalent, both at 0.7–0.9 cm, the BZ-Gel group had the largest zone diameter, which was 1.12 cm and 1.25 cm, respectively. For *E. coli*. strains, the diameter of the inhibition zone of Gel, Z-Gel, B-Gel, and BZ-Gel groups were about 1.0 cm. The above results proved that Gel had an inhibitory effect on *S. aureus* and *E. coli* but not on *S. epidermidis*. The quaternary ammonium salt produced during the degradation of pure Gel endows its antibacterial effect. Therefore, by loading Zn-BTB and BR components, the as-prepared composite hydrogel was endowed with an expanded antibacterial spectrum and enhanced antibacterial activity.

The pro-proliferative and pro-migratory effects of BZ-Gel hydrogel scaffold

The CCK-8 method was used to evaluate the biocompatibility of nanoparticles to human skin fibroblasts (HSF) and HaCaT. As shown in Figures 5A and 5B, when the concentration of BTB ligand was increased to 80 μg/mL, the cell viability of HSF and HaCaT was still close to 100%, indicating that H_3BTB possessed favorable biocompatibility. When the concentration of Zn-BTB reached 70 μg/mL, the cell viability of the two cells was still greater than 80%. It could be speculated that part of the cell toxicity was caused by the continuous accumulation of Zn^{2+} released by the slow disintegration of Zn-BTB in the culture medium. In contrast, when the concentration of BR reached 20 μg/mL, the cell viability of HSF and HaCaT were less than 60% and 80%, respectively, and they had obvious cytotoxicity against both cells. When the concentration of BR@Zn-BTB reached 60 μg/mL (with the corresponding BR concentration greater than 20 μg/mL), the viability of the cells remained above 80%. It can be inferred that by loading BR on Zn-BTB, the sudden release of BR was effectively controlled, which was beneficial to reducing the contact toxicity of BR and increasing the bioavailability of BR. The concentration of Zn-BTB and BR@Zn-BTB was adjusted to 40 μg/mL, consistent with the concentration of nanoparticles loaded in the BZ-Gel hydrogel, and these materials were used for subsequent studies.

Re-epithelialization is a key process of wound healing and requires a new epithelial surface, in addition to proper migration and proliferation of fibroblasts and keratinocytes around the wound.[44] CCK-8 assay was used to detect the long-term cytotoxicity and pro-proliferative of Zn-BTB and BR@Zn-BTB in HSF cell and HaCaT cell at safe concentrations (40 μg/mL). As shown in Figures 5E and 5F, for the two types of cells, the optical density (OD) values showed no significant difference for Zn-BTB, BR@Zn-BTB, and control groups on day 1. On day 2, for HSF cells, there was no significant difference in the OD values among the three groups. However, for HaCaT cells, the OD values of the BR@Zn-BTB group were significantly higher than that of the other groups. On day 3, for both HSF and HaCaT cells, the OD values of the BR@Zn-BTB group were significantly higher than that of the control and Zn-BTB groups.

To verify the biocompatibility of Gel, Z-Gel, and BZ-Gel, a live-dead staining method was used. As shown in Figures 5C and 5D, for both HaCaT and HSF cells, there were no significant differences in the numbers among the four groups on days 1 and 2. Notably, on day 3, the number of HaCaT and HSF cells was more than those of the control for the Gel, Z-Gel, and BZ-Gel groups. These results show that Gel, Z-Gel, and BZ-Gel exhibit good biocompatibility. In the healing process, multiple cells are required to

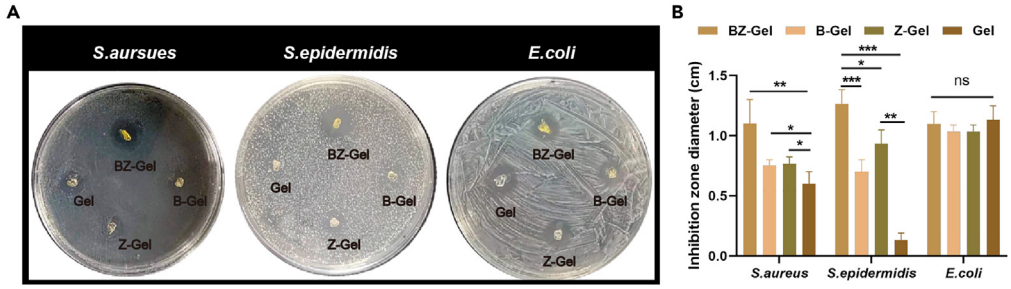

Figure 4. The antimicrobial characteristics of BZ-Gel

(A) Disc diffusion studies of the Gel, Z-Gel, B-Gel, and BZ-Gel hydrogel against *S. aureus*, *S. epidermidis*, and *E. coli*.

(B) Quantitative analysis of the antibacterial activity *in vitro*.

migrate to the wound site to participate in wound healing. Here, the scratch assay was used to evaluate the effects of the BZ-Gel hydrogel scaffold on pro-migration under a high-glucose environment (13.5 g/L).[45] For HSF cells (Figure 5G), the scratch distance in the BZ-Gel group was the smallest, then followed by Z-Gel after 48 h. There were no obvious differences in the scratch distance between the control and Gel groups. For HaCaT cells (Figure 5H), the scratch distance in the BZ-Gel group was smaller than in the control, Gel, and Z-Gel groups and there was no difference in the latter three groups. The results showed that Z-Gel promoted the migration of HSF, but it did not promote the proliferation of HaCaT. Compared with the Z-Gel group, the BZ-Gel hydrogel scaffold significantly promoted the migration of HSF and HaCaT cells. BZ-Gel hydrogel had good compatibility with skin cells and the ability to promote skin cell proliferation and migration, and have great potential in promoting diabetic skin wound healing. In the BZ-Gel group, BR and Zn^{2+} released by BZ-Gel can synergistically promote cell proliferation and migration.

In vitro antioxidant and anti-inflammatory effects, and the influence on MMP-9 gene expression of BZ-Gel hydrogel scaffold

Due to the defense mechanism, the wound site of diabetic patients may produce excessive ROS.[11] Excessive production of ROS or continuous oxidative stress can lead to cell necrosis, local acute tissue damage, or chronic inflammation.[46] To tackle these obstacles, we synthesized the BZ-Gel with the ROS scavenging effect. In this study, DCFH-DA was used to verify the antioxidant capacity of BZ-Gel. As shown in Figure 6A and fluorescence readings (Figure S5), the green fluorescence of the BZ-Gel group was the weakest among Z-Gel, Gel, and control groups, indicating that the BZ-Gel hydrogel scaffold has a good ability of scavenging ROS.

Inflammation is a normal part of the wound healing process. However, in chronic wounds, pro-inflammatory macrophages persist without changing to an anti-inflammatory phenotype, which severely inhibits tissue repair.[47] LPS is a component of the outer wall of Gram-negative bacteria, composed of lipids and polysaccharides. The cellular inflammatory response stimulated by LPS is believed to be caused by the classic NF-κB pathway.[48] In this study, LPS was used to stimulate RAW264.7, and qRT-PCR was used to detect the expression levels of inflammatory factors and evaluate the anti-inflammatory ability of BZ-Gel in which the loaded BR and Zn^{2+} can play an anti-inflammatory effect. As shown in Figures 6B–6D, the expression of IL-1β, IL-6, and TNF-α in the group without LPS stimulation was lower than in the group with LPS stimulation. The results indicated that the stimulation of LPS successfully activated the inflammatory pathway. There was no difference between the LPS-stimulated group and the Gel group. In the Z-Gel group only the inflammatory factor IL-6 was decreased compared with the LPS-stimulated group. Compared with the LPS-stimulated group, the expressions of inflammatory factors IL-1β, IL-6, and TNF-α in the BZ-Gel group were significantly decreased. The results showed that Z-Gel can inhibit the expression of inflammatory factor IL-6, and BZ-Gel can inhibit the expression of inflammatory factor IL-6, IL-1β, and TNF-α.

It is well-established that the over-expression of MMP-9 leads to a decrease in the ratio of TIMP-1/MMP-9, which seriously hinders the healing of diabetic wounds.[49,50] As shown in Figure S6, the expression of MMP-9 in HaCaT cells in a high-glucose culture environment (13.5 g/L) is higher than that in a normal environment. Herein, the influence of BZ-Gel on the expression of MMP-9 and TIMP-1 in HaCaT cells under a high-glucose environment was analyzed by qRT-PCR. As shown in Figure 6E, the expression of MMP-9 in

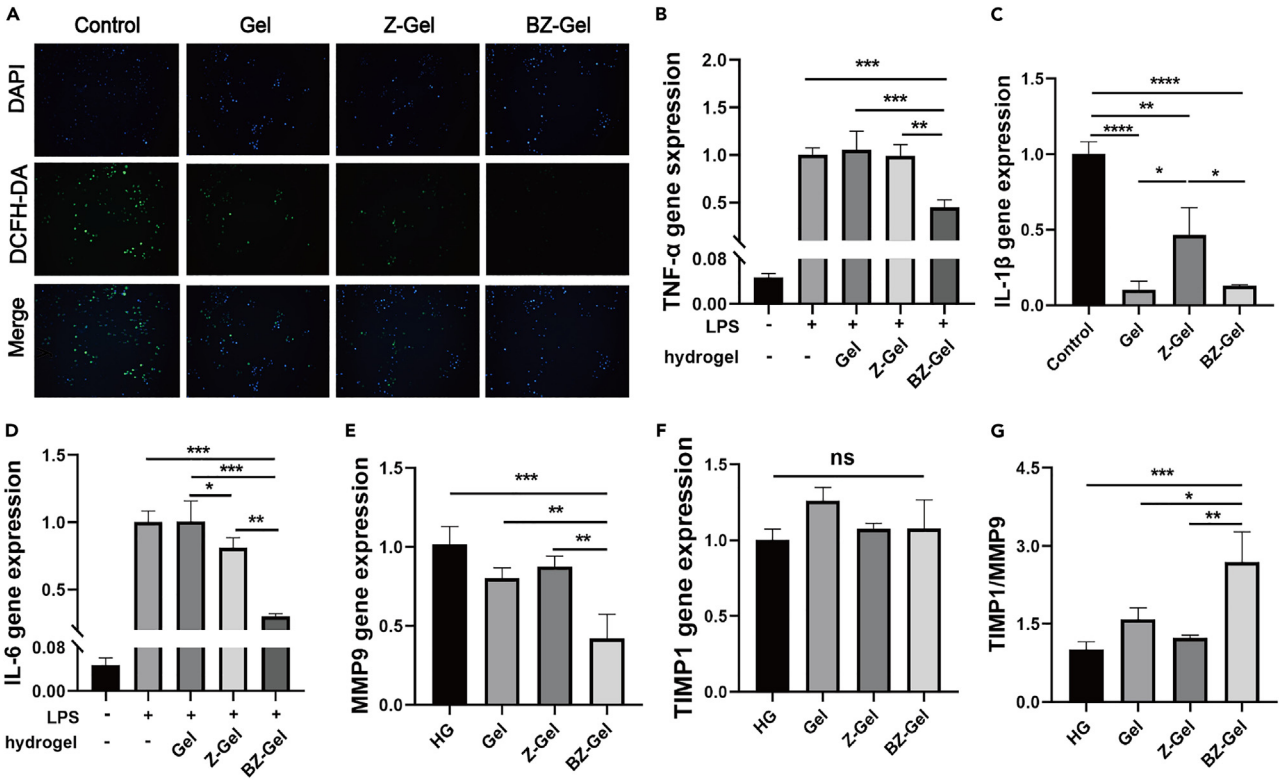

Figure 5. The cell viability and proliferative activity of BZ-Gel

(A–F) Cell viability of (A) HSF and (B) HaCaT cells cultured with H_3BTB, BR, Zn-BTB, and BR@Zn-BTB evaluated by CCK-8 assay. Cell viability of (C) HSF and (D) HaCaT cells cultured with Gel, Z-Gel, and BZ-Gel. Proliferative activity of (E) HSF and (F) HaCaT cells cultured with Zn-BTB and BR@Zn-BTB evaluated by CCK-8 assay on days 1, 2, and 3, respectively. Representative images of the scratch method of (G) HSF and (H) HaCaT cells after culturing with Gel, Z-Gel, and BZ-Gel for 48 h.

the BZ-Gel group was significantly lower than that of the control, Gel, and Z-Gel groups. There was no difference in the expression of TIMP-1 in each group (Figure 6F). However, as shown in Figure 6G, the ratio of TIMP-1/MMP-9 was significantly different. The ratio of TIMP-1/MMP-9 for the BZ-Gel group is higher than in other groups. The above results proved that BZ-Gel hydrogel can effectively inhibit the expression of MMP-9 in diabetic wounds, increase the ratio of TIMP-1/MMP-9, and promote diabetic wound healing.

The BZ-Gel hydrogel scaffold accelerating diabetic wound healing *in vivo*

The effect of the BZ-Gel hydrogel scaffold on diabetic wound healing *in vivo* was investigated by using the STZ-induced diabetic mice model. As shown in Figure 7A, the skin wounds of diabetic mice (φ = 10 mm) gradually healed within the experimental time, and the healing rate of the BZ-Gel hydrogel scaffold was significantly higher than those of the other groups. The simulation of the wound healing process (Figure 7B) intuitively shows the changes in the wound area, where the blue area was the wound area on day 0, and the purple area on day *x* (*x* = 5, 9, and 12). As shown in Figure 7C, the statistical data of wound healing showed that, on day 5, there was no significant difference in the change of wound area of each component. On day 9, the skin wound healing area of the BZ-Gel group (75.2%) was significantly higher than that of the Z-Gel group (69.5%), Gel group (67.5%), and control group (61.1%). On day 12, the skin wound healing rate of the BZ-Gel group (93.3%) was significantly higher than that of the Z-Gel group (92.5%), Gel group (91.0%), and control group (85.2%). The results above indicated that the BZ-Gel scaffold can effectively promote wounds healing in diabetic mice.

The effect of BZ-Gel hydrogel scaffold suppressing inflammatory factors in diabetic wound

H&E histological staining was used to further evaluate the degree of wound healing. As shown in Figures 8A and 8B, consistent with results observed *in vitro*, for the BZ-Gel group, the un-repaired part was shorter (red arrow) than that of Z-Gel, Gel, and control at days 9 and 12. Compared with day 9, the skin tissue wound

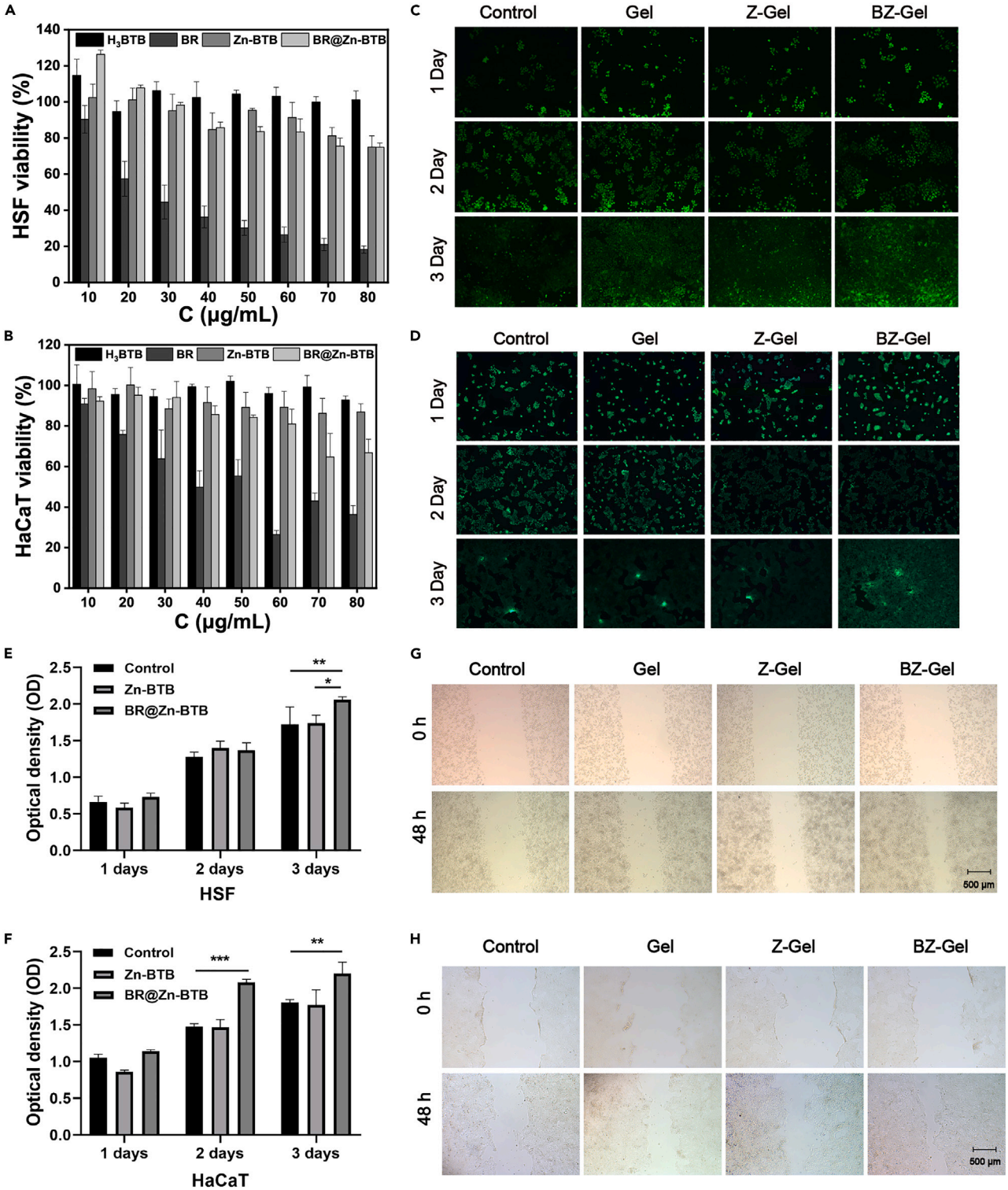

Figure 6. The effect of BZ-Gel on clearing ROS, inhibiting inflammation, and inhibiting MMP-9 expression

(A–G) (A) DCFH-DA staining of HSF cells cultured with H_2O_2 (100 μM) for 24 h with Gel, Z-Gel, and BZ-Gel and imaged by inverted fluorescence microscope. The expression levels of (B) TNF-α, (C) IL-1β, and (D) IL-6 assessed by qRT-PCR analysis. The expression levels of (E) MMP-9, (F) TIMP-1, and (G) TIMP-1/MMP-9 assessed by qRT-PCR analysis.

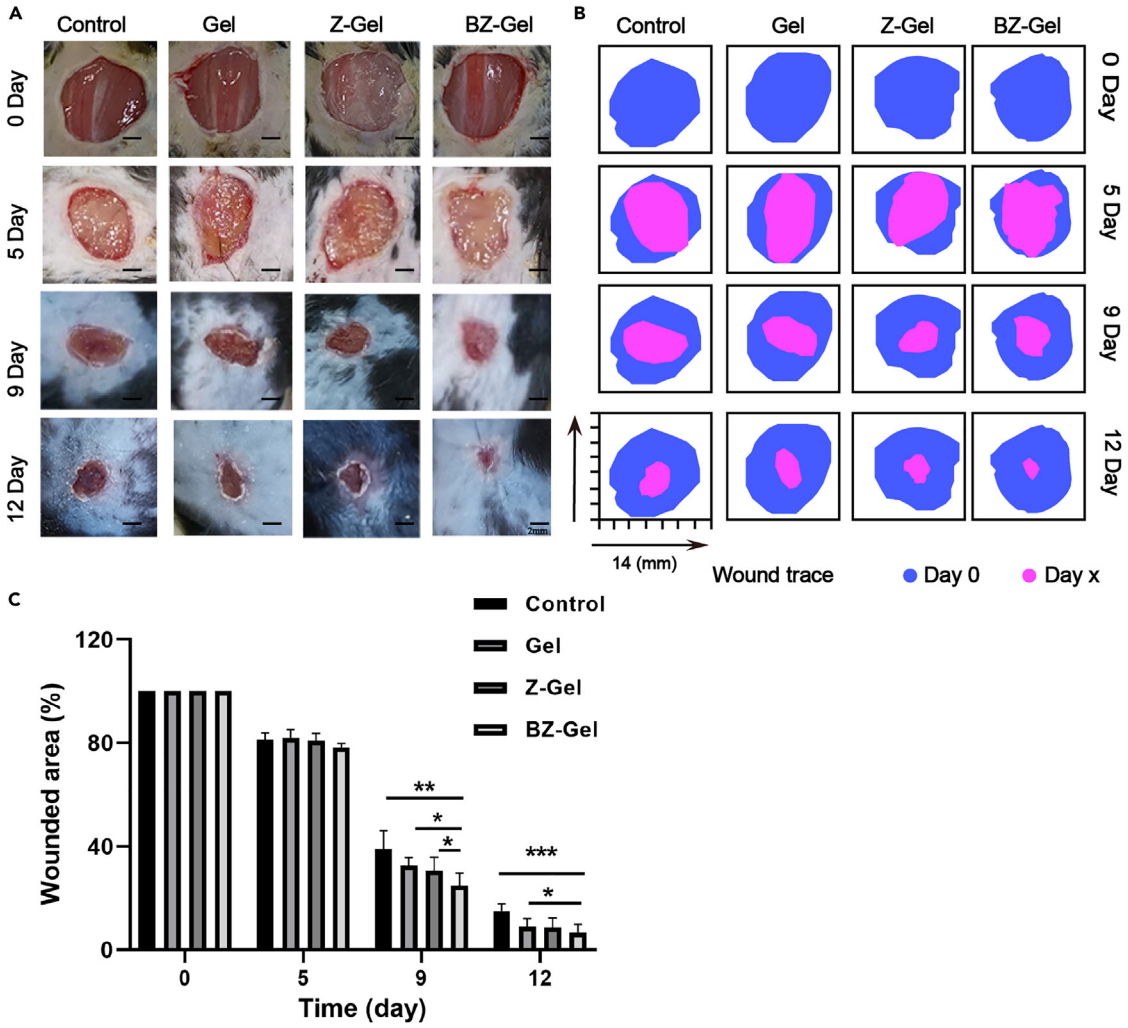

Figure 7. The effect of BZ-Gel on the diabetic mice wound healing

(A) The size change of back skin resection in diabetic mice at different periods.

(B) Simulation of wound bed closure trace in each group *in vivo*. The blue area represented the wound area on day 0 and the purple area represented the area of the wound on day *x* (*x* = 5, 9, and 12).

(C) The wound area of the four groups statistically analyzed to show the healing effect.

space on day 12 had certain shrinkage, and some skin appendages have grown. It could be seen from the enlarged part that the cells in the control group are dense, with most of them featuring inflammatory cells, while the BZ-Gel group had relatively few cells and accordingly fewer inflammatory cells. Moreover, as shown in Figures 8C–8E, compared with the control group, the gene expression of TNF-α, IL-1β, and IL-6 in the Gel, Z-Gel, and BZ-Gel groups was significantly down-regulated, especially for the BZ-Gel group. By increasing the biocompatibility of materials, immune rejection and the production of inflammatory factors can be reduced.[51] In addition, several reports have shown that BR has anti-inflammatory effects on different inflammatory diseases. The main mechanism is that BR can inhibit the activation of NLRP3 inflammasomes by inducing mitochondrial autophagy and reducing mitochondrial ROS, thereby inhibiting TNF-α and IL-1β, and IL-6 gene expression.[52] The above results indicate that BZ-Gel can inhibit wound inflammation and promote wound healing.

The effect of BZ-Gel hydrogel scaffold on promoting collagen deposition and inhibiting the expression of MMP-9

The deposition and remodeling of collagen are beneficial to enhance tissue tensile strength and promote wound healing.[53] Therefore, Masson's trichrome staining test was performed to evaluate collagen

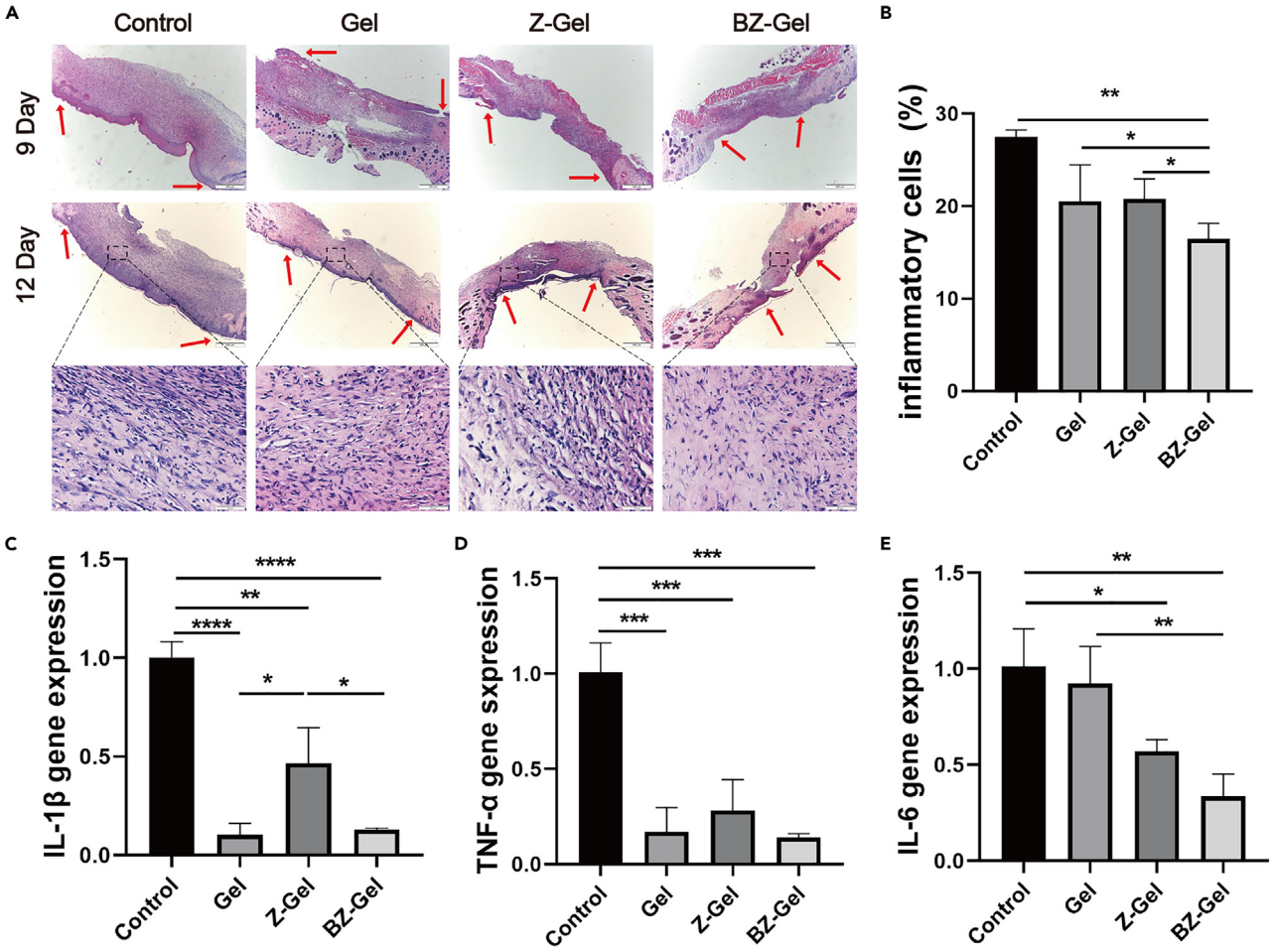

Figure 8. The effect of BZ-Gel on anti-inflammatory in diabetic mice

(A) Histological evaluation of H&E staining for the newly grown epithelium in the control, Gel, Z-Gel, and BZ-Gel groups at days 9 and 12 (bar:500 μm, 50 μm).

(B) Quantitative analysis of inflammatory cells.

(C–E) The expression levels of (C) IL-1β, (D) TNF-α, and (E) IL-6 assessed by qRT-PCR on day 12.

deposition in diabetic wounds. As shown in Figures 9A and 9B, on day 12, the BZ-Gel collagen blue staining area is large with deep color, while that of the control group is small with light color. This indicates the coverage of the collagen in the BZ-Gel group was higher. qRT-PCR was used to detect the expression of MMP-9 in the skin tissue of mice to detect the effect of BZ-Gel hydrogel on MMP-9. As shown in Figures 9C–9E, the expression of MMP-9 was decreased, and the expression of TIMP-1 was increased and with the ratio of TIMP-1 to MMP-9 also higher than that of the control group. This is inconsistent with the results of cell experiments, because the results were obtained under the condition that the inflammation has been relieved. Long-term inflammation is one of the main reasons that hinder the healing of diabetic wounds. Previous studies have shown that the expression of MMP-9 was very low under steady-state conditions and could be activated by the over-expression of pro-inflammatory factors such as IL-6 and IL-1β.[16] With the improvement of wound inflammation, the expression of MMP-9 will decrease, and the expression of TIMP-1 will increase.[54] Therefore, after the wound inflammation was improved, the expression of MMP-9 and TIMP-1 on the wound will also progress in the direction of promoting wound healing. Overall, the above results indicated that BZ-Gel hydrogel significantly accelerated wound healing by promoting collagen deposition and inhibiting MMP-9 expression.

Conclusions

In this work, an ROS-responsive hydrogel encapsulating BR@Zn-BTB nanoparticles was developed to promote diabetic wound healing by eliminating ROS, inhibiting inflammatory factors, and the over-expression

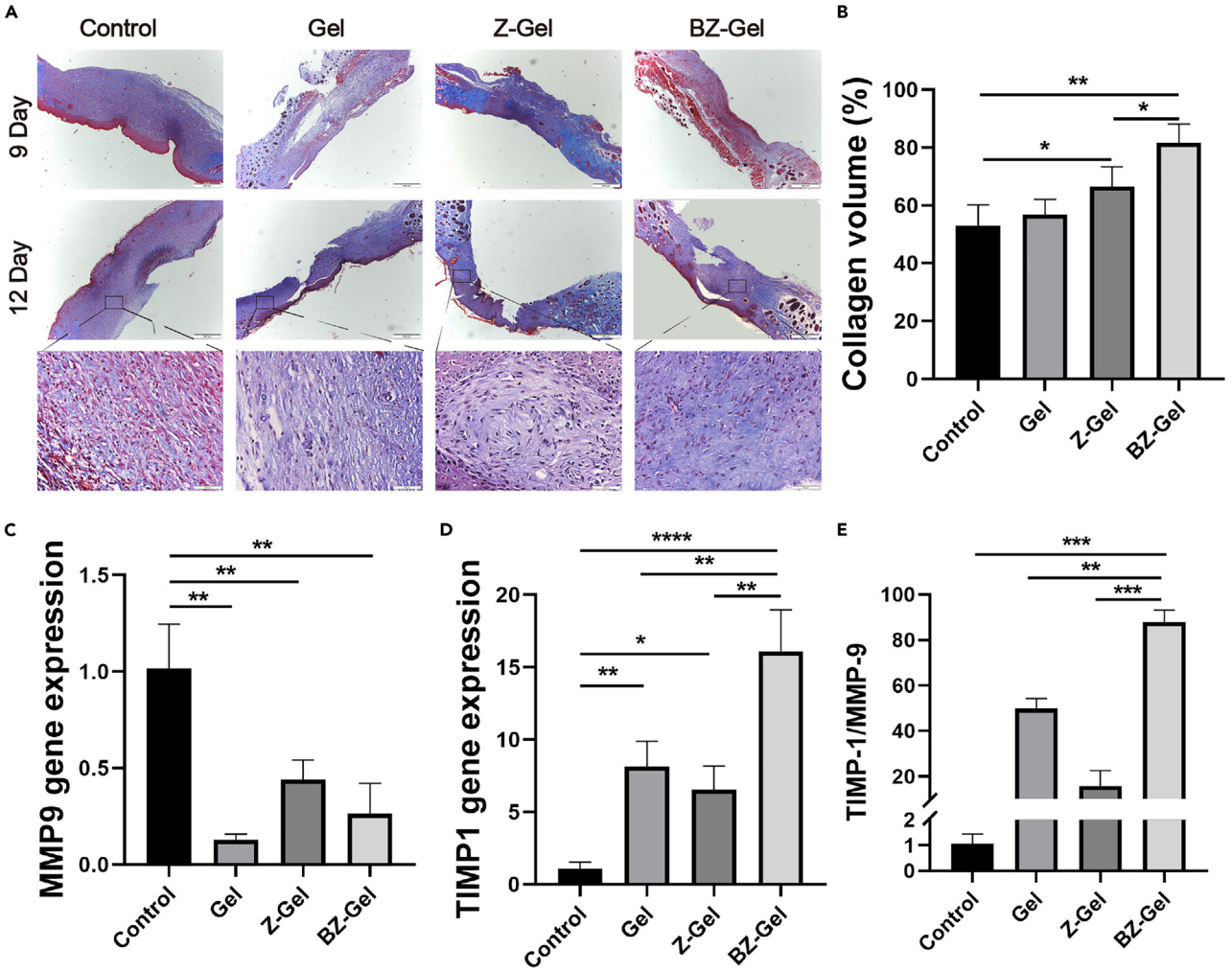

Figure 9. The effect of BZ-Gel on collagen deposition in diabetic mice

(A) Histological evaluation of Masson's trichrome staining for the diabetic wound beds collagen deposition in the control, Gel, Z-Gel, and BZ-Gel groups at days 9 and 12 (the blue part represents collagen fibers, and the red part represents muscle fibers) (bar:500 μm, 50 μm).

(B) Quantitative analysis of collagen.

(C–E) The expression levels of (C) MMP-9, (D) TIMP-1, and (E) TIMP-1/MMP-9 assessed by qRT-PCR analysis of back skin resection in diabetic mice on day 12.

of MMP-9. The results showed that the Zn-based NMOF with BTB as the ligand has a high BR-loading capacity of about 350 mg/g and achieves a controlled release of BR and Zn^{2+}. *In vitro* experiments show that the composite hydrogel can eliminate ROS, and the released Zn^{2+} and BR could be anti-inflammatory and inhibit the expression of MMP-9 and promote skin cell proliferation and migration. In addition, the composite hydrogel dressing showed the synergistic antibacterial effect of BR and Zn^{2+} in the antibacterial experiment *in vitro*. The *in vivo* results further show that BZ-Gel could inhibit the inflammation of the skin tissue of the diabetic wound enhance the deposition of collagen, and ultimately promote the healing of the wound of diabetic mice. This study showed that the ROS-responsive hydrogel dressing encapsulated with BR@Zn-BTB provides a new strategy for promoting diabetic wound healing.

STAR★METHODS

Detailed methods are provided in the online version of this paper and include the following:

- KEY RESOURCES TABLE
- RESOURCE AVAILABILITY
  - Lead contact

SUPPLEMENTAL INFORMATION

Supplemental information can be found online at https://doi.org/10.1016/j.isci.2023.106775.

ACKNOWLEDGMENTS

We thank Xiaoyan Tang for her help with the characterization of materials and Fuzheng Feng, and Yekai Zhou for their help with modeling diabetic mice. This work was supported by the National Natural Science Foundation of China (81974328, 21874064, 22004059, and 21871203), the Natural Science Foundation from Guangdong Science and Technology Department of China (2018A030313456), Science and Technology Program of Guangzhou (201904010410 and 202102020640), The Medical Science and Technology Research Fund of Guangdong Province (B2021272). The Medical Science and Technology Research Fund Project of Guangdong Province (A2020387). The Basic and Applied Basic Research Project of Guangzhou Basic Research Program (202201011600).

AUTHOR CONTRIBUTIONS

H. J. J. (First Author): Conceptualization, Methodology, Data Curation, Formal Analysis, Visualization, Writing - Original Draft; Y. X. Z. (First Author): Conceptualization, Methodology, Validation, Writing - Original Draft; Z. S. Q.: Visualization, Conceptualization, Funding Acquisition; Y-X. Z.: the revision for the manuscript format; C. X. L.: Resources; L. Z. J.: Investigation; H. Z. H.: Funding Acquisition; X. D. H.: Funding Acquisition, Writing-Review & Editing; Z. W.-H.: Software; C. J.-X. (Corresponding Author): Project Administration, Writing-Review & Editing, Funding Acquisition; Z. Q. (Corresponding Author): Project administration, Supervision, Funding Acquisition, Writing-Review & Editing.

DECLARATION OF INTERESTS

The authors of this study declare that there is no conflict of interest.

INCLUSION AND DIVERSITY

We support inclusive, diverse, and equitable conduct of research.

Received: February 28, 2022
Revised: April 4, 2023
Accepted: April 25, 2023
Published: April 29, 2023

REFERENCES

1. Jeffcoate, W.J., Vileikyte, L., Boyko, E.J., Armstrong, D.G., and Boulton, A.J.M. (2018). Current challenges and opportunities in the prevention and management of diabetic foot ulcers. Diabetes Care *41*, 645–652.

2. Hoffstad, O., Mitra, N., Walsh, J., and Margolis, D.J. (2015). Diabetes, lower-extremity amputation, and death. Diabetes Care *38*, 1852–1857.

3. Brennan, M.B., Hess, T.M., Bartle, B., Cooper, J.M., Kang, J., Huang, E.S., Smith, M., Sohn, M.W., and Crnich, C. (2017). Diabetic foot ulcer severity predicts mortality among veterans with type 2 diabetes. J. Diabetes Complication *31*, 556–561.

4. Rice, J.B., Desai, U., Cummings, A.K.G., Birnbaum, H.G., Skornicki, M., and Parsons, N.B. (2014). Burden of diabetic foot ulcers for medicare and private insurers. Diabetes Care *37*, 651–658.

5. Dixon, D., and Edmonds, M. (2021). Managing diabetic foot ulcers: pharmacotherapy for wound healing. Drugs *81*, 29–56.

6. Bowling, F.L., Rashid, S.T., and Boulton, A.J.M. (2015). Preventing and treating foot complications associated with diabetes mellitus. Nat. Rev. Endocrinol. *11*, 606–616.

7. Whitney, J.D. (2005). Overview: acute and chronic wounds. Nurs. Clin. North Am. *40*, 191–205.

8. Burgess, J.L., Wyant, W.A., Abdo Abujamra, B., Kirsner, R.S., and Jozic, I. (2021). Diabetic wound-healing science. Medicina *57*, 1072.

9. Patel, S., Srivastava, S., Singh, M.R., and Singh, D. (2019). Mechanistic insight into diabetic wounds: pathogenesis, molecular targets and treatment strategies to pace wound healing. Biomed. Pharmacother. *112*, 108615.

10. Deng, L., Du, C., Song, P., Chen, T., Rui, S., Armstrong, D.G., and Deng, W. (2021). The role of oxidative stress and antioxidants in diabetic wound healing. Oxid. Med. Cell. Longev. *2021*, 1–11.

11. Kunkemoeller, B., and Kyriakides, T.R. (2017). Redox signaling in diabetic wound healing regulates extracellular matrix deposition. Antioxid. Redox Signal. *27*, 823–838.

12. Qian, B., Li, J., Guo, K., Guo, N., Zhong, A., Yang, J., Wang, J., Xiao, P., Sun, J., and Xiong, L. (2021). Antioxidant biocompatible composite collagen dressing for diabetic wound healing in rat model. Regen. Biomater. *8*, rbab003.

13. Yabluchanskiy, A., Ma, Y., Iyer, R.P., Hall, M.E., and Lindsey, M.L. (2013). Matrix metalloproteinase-9: many shades of function in cardiovascular disease. Physiology *28*, 391–403.

14. Liu, Y., Min, D., Bolton, T., Nubé, V., Twigg, S.M., Yue, D.K., and McLennan, S.V. (2009). Increased matrix metalloproteinase-9 predicts poor wound healing in diabetic foot ulcers. Diabetes Care *32*, 117–119.

15. Rayment, E.A., Upton, Z., and Shooter, G.K. (2008). Increased matrix metalloproteinase-9 (MMP-9) activity observed in chronic wound fluid is related to the clinical severity of the ulcer. Br. J. Dermatol. *158*, 951–961.

16. Chang, M., and Nguyen, T.T. (2021). Strategy for treatment of infected diabetic foot ulcers. Acc. Chem. Res. *54*, 1080–1093.

17. Lobmann, R., Ambrosch, A., Schultz, G., Waldmann, K., Schiweck, S., and Lehnert, H. (2002). Expression of matrix-metalloproteinases and their inhibitors in the wounds of diabetic and non-diabetic patients. Diabetologia *45*, 1011–1016.

18. Wang, S., Zheng, H., Zhou, L., Cheng, F., Liu, Z., Zhang, H., Wang, L., and Zhang, Q. (2020). Nanoenzyme-reinforced injectable hydrogel for healing diabetic wounds infected with multidrug resistant bacteria. Nano Lett. *20*, 5149–5158.

19. Li, J., Lv, F., Li, J., Li, Y., Gao, J., Luo, J., Xue, F., Ke, Q., and Xu, H. (2020). Cobalt-based metal-organic framework as a dual cooperative controllable release system for accelerating diabetic wound healing. Nano Res. *13*, 2268–2279.

20. Wu, Z., and Hong, Y. (2019). Combination of the silver-ethylene interaction and 3D printing to develop antibacterial superporous hydrogels for wound management. ACS Appl. Mater. Interfaces *11*, 33734–33747.

21. Xu, M., Qi, Q., Men, L., Wang, S., Li, M., Xiao, M., Chen, X., Wang, S., Wang, G., Jia, H., and Liu, C. (2020). Berberine protects kawasaki disease-induced human coronary artery endothelial cells dysfunction by inhibiting of oxidative and endoplasmic reticulum stress. Vascul. Pharmacol. *127*, 106660.

22. Zhou, R., Xiang, C., Cao, G., Xu, H., Zhang, Y., Yang, H., and Zhang, J. (2021). Berberine accelerated wound healing by restoring TrxR1/JNK in diabetes. Clin. Sci. *135*, 613–627.

23. Jin, J., Xu, M., Liu, Y., Ji, Z., Dai, K., Zhang, L., Wang, L., Ye, F., Chen, G., and Lv, Z. (2020). Alginate-based composite microspheres coated by berberine simultaneously improve hemostatic and antibacterial efficacy. Colloid. Surface. B *194*, 111168.

24. Khan, S., Hussain, A., Attar, F., Bloukh, S.H., Edis, Z., Sharifi, M., Balali, E., Nemati, F., Derakhshankhah, H., Zeinabad, H.A., et al. (2022). A review of the berberine natural polysaccharide nanostructures as potential anticancer and antibacterial agents. Biomed. Pharmacother. *146*, 112531.

25. Xie, B.P., Qiu, G.H., Hu, P.P., Liang, Z., Liang, Y.M., Sun, B., Bai, L.P., Jiang, Z.H., and Chen, J.X. (2018). Simultaneous detection of dengue and zika virus RNA sequences with a three-dimensional Cu-based zwitterionic metal-organic framework, comparison of single and synchronous fluorescence analysis. Sensor. Actuat. B Chem. *254*, 1133–1140.

26. Qin, L., Sun, Z.Y., Cheng, K., Liu, S.W., Pang, J.X., Xia, L.M., Chen, W.H., Cheng, Z., and Chen, J.X. (2017). Zwitterionic manganese and gadolinium metal-organic frameworks as efficient contrast agents for in vivo magnetic resonance imaging. ACS Appl. Mater. Interfaces *9*, 41378–41386.

27. Zhang, Z.X., Ding, N.N., Zhang, W.H., Chen, J.X., Young, D.J., and Hor, T.S.A. (2014). Stitching 2D polymeric layers into flexible interpenetrated metal-organic frameworks within single crystals. Angew. Chem. Int. Ed. Engl. *53*, 4628–4632.

28. Lin, S., Liu, X., Tan, L., Cui, Z., Yang, X., Yeung, K.W.K., Pan, H., and Wu, S. (2017). Porous iron-carboxylate metal–organic framework: a novel bioplatform with sustained antibacterial efficacy and nontoxicity. ACS Appl. Mater. Interfaces *9*, 19248–19257.

29. Yu, P., Han, Y., Han, D., Liu, X., Liang, Y., Li, Z., Zhu, S., and Wu, S. (2020). In-situ sulfuration of Cu-based metal-organic framework for rapid near-infrared light sterilization. J. Hazard Mater. *390*, 122126.

30. Luo, Y., Li, J., Liu, X., Tan, L., Cui, Z., Feng, X., Yang, X., Liang, Y., Li, Z., Zhu, S., et al. (2019). Dual metal-organic framework heterointerface. ACS Cent. Sci. *5*, 1591–1601.

31. Li, J., Liu, X., Tan, L., Cui, Z., Yang, X., Liang, Y., Li, Z., Zhu, S., Zheng, Y., Yeung, K.W.K., et al. (2019). Zinc-doped prussian blue enhances photothermal clearance of staphylococcus aureus and promotes tissue repair in infected wounds. Nat. Commun. *10*, 4490.

32. Xiao, J., Zhu, Y., Huddleston, S., Li, P., Xiao, B., Farha, O.K., and Ameer, G.A. (2018). Copper metal–organic framework nanoparticles stabilized with folic acid improve wound healing in diabetes. ACS Nano *12*, 1023–1032.

33. Dankova, M., Domorakova, I., Fagova, Z., Stebnicky, M., Kunova, A., and Mechirova, E. (2019). Bradykinin and noradrenaline preconditioning influences level of

antioxidant enzymes SOD, CuZn-SOD, Mn-SOD and catalase in the white matter of spinal cord in rabbits after ischemia/reperfusion. Eur. J. Histochem. *63*, 197–203.

34. Yao, S., Chi, J., Wang, Y., Zhao, Y., Luo, Y., and Wang, Y. (2021). Zn-MOF encapsulated antibacterial and degradable microneedles array for promoting wound healing. Adv. Healthc. Mater. *10*, 2100056.

35. Qing, X., He, G., Liu, Z., Yin, Y., Cai, W., Fan, L., and Fardim, P. (2021). Preparation and properties of polyvinyl alcohol/N-succinyl chitosan/lincomycin composite antibacterial hydrogels for wound dressing. Carbohydr. Polym. *261*, 117875.

36. Zhou, D., Yang, R., Yang, T., Xing, M., and Luo, G. (2018). Preparation of chitin-amphipathic anion/quaternary ammonium salt ecofriendly dressing and its effect on wound healing in mice. Int. J. Nanomed. *13*, 4157–4169.

37. Wang, J., Ye, Y., Yu, J., Kahkoska, A.R., Zhang, X., Wang, C., Sun, W., Corder, R.D., Chen, Z., Khan, S.A., et al. (2018). Core-shell microneedle gel for self-regulated insulin delivery. ACS Nano *12*, 2466–2473.

38. Chen, J.X., Chen, M., Ding, N.N., Chen, W.H., Zhang, W.H., Hor, T.S.A., and Young, D.J. (2014). Transmetalation of a dodecahedral Na-9 aggregate-based polymer: a facile route to water stable Cu(II) coordination networks. Inorg. Chem. *53*, 7446–7454.

39. Saha, D., and Deng, S. (2010). Structural stability of metal organic framework MOF-177. J. Phys. Chem. Lett. *1*, 73–78.

40. He, S.B., Chen, R.T., Wu, Y.Y., Wu, G.W., Peng, H.P., Liu, A.L., Deng, H.H., Xia, X.H., and Chen, W. (2019). Improved enzymatic assay for hydrogen peroxide and glucose by exploiting the enzyme-mimicking properties of BSA-coated platinum nanoparticles. Mikrochim. Acta *186*, 778.

41. Lu, D., Zeng, Z., Geng, Z., Guo, C., Pei, D., Zhang, J., and Yu, S. (2022). Macroporous methacrylated hyaluronic acid hydrogel with different pore sizes for in vitro and in vivo evaluation of vascularization. Biomed. Mater. *17*, 025006.

42. Zhou, Y., Liu, S., Ming, J., Li, Y., Deng, M., and He, B. (2017). Sustained release effects of berberine-loaded chitosan microspheres on in vitro chondrocyte culture. Drug Dev. Ind. Pharm. *43*, 1703–1714.

43. Zhu, Y., Zhang, J., Song, J., Yang, J., Du, Z., Zhao, W., Guo, H., Wen, C., Li, Q., Sui, X., and Zhang, L. (2019). A multifunctional pro-healing zwitterionic hydrogel for simultaneous optical monitoring of pH and glucose in diabetic wound treatment. Adv. Funct. Mater. *30*, 1905493.

44. Li, D., Li, X.I., Wang, A., Meisgen, F., Pivarcsi, A., Sonkoly, E., Ståhle, M., and Landén, N.X. (2015). MicroRNA-31 promotes skin wound healing by enhancing keratinocyte proliferation and migration. J. Invest. Dermatol. *135*, 1676–1685.

45. Yan, Y., Liu, X., Zhuang, Y., Zhai, Y., Yang, X., Yang, Y., Wang, S., Hong, F., and Chen, J. (2020). Pien Tze Huang accelerated wound healing by inhibition of abnormal fibroblast apoptosis in Streptozotocin induced diabetic mice. J. Ethnopharmacol. *261*, 113203.

46. Ding, Z., Zhang, Y., Guo, P., Duan, T., Cheng, W., Guo, Y., Zheng, X., Lu, G., Lu, Q., and Kaplan, D.L. (2021). Injectable desferrioxamine-laden silk nanofiber hydrogels for accelerating diabetic wound healing. ACS Biomater. Sci. Eng. *7*, 1147–1158.

47. Xu, Z., Liang, B., Tian, J., and Wu, J. (2021). Anti-inflammation biomaterial platforms for chronic wound healing. Biomater. Sci. *9*, 4388–4409.

48. Ma, J., Shi, H., Mi, C., Li, H.L., Lee, J.J., and Jin, X. (2015). Malloapelta B suppresses LPS-induced NF-κB activation and NF-κB-regulated target gene products. Int. Immunopharmacol. *24*, 147–152.

49. Luanraksa, S., Jindatanmanusan, P., Boonsiri, T., Nimmanon, T., Chaovanalikit, T., and Arnutti, P. (2018). An MMP/TIMP ratio scoring system as a potential predictive marker of diabetic foot ulcer healing. J. Wound Care *27*, 849–855.

50. Li, G., Zou, X., Zhu, Y., Zhang, J., Zhou, L., Wang, D., Li, B., and Chen, Z. (2017). Expression and influence of matrix metalloproteinase-9/tissue inhibitor of metalloproteinase-1 and vascular endothelial growth factor in diabetic foot ulcers. Int. J. Low. Extrem. Wounds *16*, 6–13.

51. Kühne, M., Kretzer, C., Lindemann, H., Godmann, M., Heinze, T., Werz, O., and Heinzel, T. (2021). Biocompatible valproic acid-coupled nanoparticles attenuate lipopolysaccharide-induced inflammation. Int. J. Pharm. *601*, 120567.

52. Liu, H., You, L., Wu, J., Zhao, M., Guo, R., Zhang, H., Su, R., Mao, Q., Deng, D., and Hao, Y. (2020). Berberine suppresses influenza virus-triggered NLRP3 inflammasome activation in macrophages by inducing mitophagy and decreasing mitochondrial ROS. J. Leukoc. Biol. *108*, 253–266.

53. Chouhan, D., Dey, N., Bhardwaj, N., and Mandal, B.B. (2019). Emerging and innovative approaches for wound healing and skin regeneration: current status and advances. Biomaterials *216*, 119267.

54. Ambrosch, A., Halevy, D., Fwity, B., Brin, T., and Lobmann, R. (2014). Effect of daptomycin on local interleukin-6, matrix metalloproteinase-9, and metallopeptidase inhibitor 1 in patients with MRSA-infected diabetic foot. Int. J. Low. Extrem. Wounds *13*, 12–16.

55. Sonamuthu, J., Cai, Y., Liu, H., Kasim, M.S.M., Vasanthakumar, V.R., Pandi, B., Wang, H., and Yao, J. (2020). MMP-9 responsive dipeptide-tempted natural protein hydrogel-based wound dressings for accelerated healing action of infected diabetic wound. Int. J. Biol. Macromol. *153*, 1058–1069.

STAR★METHODS

KEY RESOURCES TABLE

REAGENT or RESOURCE	SOURCE	IDENTIFIER
Bacterial and virus strains		
Staphylococcus aureus	BNCC	BNCC186067
Staphylococcus epidermidis	BNCC	BNCC185917
Escherichia coli	BNCC	BNCC336902
Chemicals, peptides, and recombinant proteins		
$ZnCl_2$	Macklin	Z820755; CAS: 7646-85-7
Berberin hydrochloride	Macklin	B875003; CAS: 2086-83-1
H_3BTB	Macklin	T833353-1g CAS: 50446-44-1
Poly (vinyl alcohol)	Macklin	P914585; CAS: 9002-89-5
Tetramethyl-1,3-diaminopropane	Macklin	N819128; CAS: 110-95-2
4-(Bromomethyl)phenylboronic acid	Macklin	B803441; CAS: 68162-47-0
Dimethylformamide	Macklin	N807505; CAS: 25174
DCFH-DA	Sigma-Aldrich	D6883-50; CAS: 4091-99-0
Streptozotocin	Sigma-Aldrich	S0130; CAS:18883-66-4
fetal bovine serum	Gibco	A316802
Dulbecco's modified eagle medium	Gibco	C11995500BT
Pancreatin	Gibco	25200056
Trizol	Life Technologies	15596026
TB Green™ Premix Ex Taq™ II	TaKaRa	RR820A
Critical commercial assays		
CCK-8	Beyotime	C0037
LIVE/DEAD® Cell Imaging Kit	Beyotime	C2015S
Hematoxylin and Eosin Staining Kit	Solarbio	G1120-100
Masson's Trichrome Stain Kit	Solarbio	G1340
Experimental models: Cell lines		
Human: HSF cells	NEWGAINBIO	CH1178-1
Human: HaCat cells	NEWGAINBIO	CH1031-1
mice: RAW264.7	NEWGAINBIO	CM3034
Oligonucleotides		
Primers for qRT-PCR of MMP-9 mRNA (Human): (F)5′GGACCCGAAGCGGACATTG; (R)5′ CGTCGTCGAAATGGGCATCT	TSINGKE	None

(*Continued on next page*)

Continued

REAGENT or RESOURCE	SOURCE	IDENTIFIER
Primers for qRT-PCR of TIMP-1 mRNA (Human): (F)5′ CTTGGTTCCCTGGCGTACTC; (R)5′ ACCTGATCCGTCCACAAACAG	TSINGKE	None
Primers for qRT-PCR of actin mRNA (Human): (F)5′ GCCGGGACCTGACTGACTAC; (R)5′ TTCTCCTTAATGTCACGCACGAT	TSINGKE	None
Primers for qRT-PCR of MMP-9 mRNA (Human): (F)5′ CATTCGCGTGGATAAGGAGT; (R)5′ TCACACGCCAGAAGAATTTG	TSINGKE	None
Primers for qRT-PCR of TIMP-1 mRNA (Mouse): (F)5′ CGAGACCACCTTATACCAGCG; (R)5′ ATGACTGGGGTGTAGGCGTA	TSINGKE	None
Primers for qRT-PCR of IL-6 mRNA (Mouse): (F)5′ GGAGCCCACCAAGAACGATA; (R)5′ ACCAGCATCAGTCCCAAGAA	TSINGKE	None
Primers for qRT-PCR of TNF-α mRNA (Mouse): (F)5′ CTCATGCACCACCATCAAGG; (R)5′ ACCTGACCACTCTCCCTTTG	TSINGKE	None
Primers for qRT-PCR of IL-1β mRNA (Mouse): (F)5′ ATGAAGGGCTGCTTCCAAAC; (R)5′ TCTCCACAGCCACAATGAGT	TSINGKE	None
Primers for qRT-PCR of GAPDH mRNA (Mouse): (F)5′ GGGTCCCAGCTTAGGTTCAT; (R)5′ CCAATACGGCCAAATCCGTT	TSINGKE	None
Software and algorithms		
Image J	NIH	https://imagej.nih.gov/ij/download.html
Origin	OriginLab	https://www.originlab.com
GraphPad Prism	GraphPad	https://www.graphpad.com/
Other		
Field-emission scanning electron microscopy, FE-SEM	GeminiSEM	sigma 500; https://www.zeiss.com.tw/microscopy/local-content/
Zeta-sizer Nano ZS,	Malvern	Zeta-sizer Nano ZS; https://somf.engr.tamu.edu/zetasizer
Powder X-ray Diffraction, PXRD	Rigaku	D/MAX-2200; https://www.rigaku.com/products/xrd
Fourier Transform infrared spectroscopy, FT-IR	PerkinElmer	Frontier FT-IR/NIR/FIR; https://chem.washington.edu/instruments/perkin-elmer-frontier-ftir
Nuclear Magnetic Resonance, NMR	BRUKER	AVANCE-III HD 400 MHz; https://pharm.ucsf.edu/nmr/instruments/bruker-400
Inductively Coupled Plasma Mass spectrometry, ICP-MS	PerkinElmer	Optima 7000 DV; https://www.labx.com/product/perkinelmer-optima-7000-dv
Ultraviolet–visible spectroscopy, UV-Vis	Perkin Elmer	LS55 UV-Vis spectrometer; https://www.spectralabsci.com/equipment/perkin.

RESOURCE AVAILABILITY

Lead contact

Further information and requests for resources and reagents should be directed to and will be fulfilled by the lead contact, Qun Zhang (zq1979@smu.edu.cn).

Materials availability

This study did not generate new unique reagents.

Data and code availability

Data reported in this paper will be shared by the lead contact upon request.

This paper does not report original code.

Any additional information required to reanalyze the data reported in this paper is available from the lead contact upon request.

EXPERIMENTAL MODEL AND SUBJECT DETAILS

Diabetic mice model

The experimental animals in this study were purchased from the Guangdong Provincial Animal Center, and the animal experiments were approved by the Guangdong Provincial Animal Ethics Committee. The diabetic mice were induced by streptozotocin (STZ) according to previous reports.[55] Briefly, male mice aged 6–8 weeks were intraperitoneally injected with STZ at a dose of 50 mg/kg for 5 consecutive days. 2 weeks after STZ injection, the blood glucose value of the tail tip of the mice was measured, and the blood glucose at the two random times was not less than 300 mg/dL (16.7 mmol/L).

Cell line culture

Human skin fibroblasts (HSF) and human immortalized keratinocytes (HaCaT) cells were cultured in DMEM medium with the supplementation of 10% (v/v) FBS and 100 units/mL Penicillin/Streptomycin (GIBCO). RAW264.7 cells were cultured in DMEM (GIBCO) medium with the supplementation of 20% (v/v) FBS. The cells were cultured under 5% CO_2 at 37°C.

High-glucose environmental cell model

D-glucose was added to DMEN medium to prepare a high-glucose medium with a concentration of 13.5 g/L, and then filtered through a sterile microporous filter head (PES13x0.22). The cells were seeded in petri dishes. After 12 h, remove the supernatant and add the prepared high-glucose medium.

Inflammatory cell model

AW264.7 cells was seeded in a petri dish. After the cells adhered, the supernatant was removed, washed twice with PBS. Then, DMEN medium with lps concentration of 500 ng/ml was added and stimulated for 12 h.

METHOD DETAILS

Material characterization

The material morphology was observed using field-emission scanning electron microscopy (FE-SEM, sigma 500). The particle size was estimated by the dynamic light particle size analyzer (Zeta-sizer Nano ZS, Malvern, UK). Powder X-ray diffraction (PXRD) patterns were recorded at a rate of $2^{\circ}\cdot min^{-1}$ in the range of 5–40° (PXRD, D/max-2200/PC). The functional groups of the samples were further determined by Fourier transform infrared spectra (FT-IR, Frontier, USA) in the wavenumber range of 4000−400 cm^{-1}. The Ultraviolet-visible (UV-Vis) spectroscopy was measured on a Perkin Elmer LS55 UV-vis spectrometer. The structure of TPA was measured by ^{1}H NMR on Bruker (Swiss) AVANCE III (400 MHz). The scanning electron microscope (SEM) image of hydrogel was acquired by field-emission SEM of Phenom PRO. The release process of Zn^{2+} was detected by inductive coupled plasma atomic emission spectrometry (ICP-MS) (ICPAES, Perkin-Elmer Optima 7000 DV).

Calculation method of drug loading rate of berberine by UV-vis spectroscopy according to the standard curve method

First, precisely weighed a certain mass of BR@Zn-BTB(M) and disintegrated it with a strong alkaline solution. Then measure the ultraviolet absorption of berberine in the solution, and calculate the mass (m) of berberine through the standard curve (see Figure S2). Loading rate of berberine = m/M*100%.

Exploring the synthesis conditions of BR@Zn-BTB nanoparticles by orthogonal reaction

First, the effect of reaction time on particle size and loading rate of BR was explored. Weigh H_3BTB (60 mg) and $ZnCl_2$ (22.74 mg), respectively, dissolve in 18 mL of DMF solution containing saturated concentration of berberine, dissolve by sonication, then mix and transfer the mixture to a hydrothermal tube at 80°C, and reacted for 6 days. Take 3 mL every day, centrifuge at 10,000 rpm for 5 min, and wash with methanol 3 times. Take an appropriate amount of precipitate, re-disperse it with DMF, and measured the particle size with a particle size analyzer. The remainder was dried and weighed in the appropriate mass. Soluble in strong alkaline solution, and then detected the absorbance of the solution with UV. Calculate the loading rate of berberine. Then, the effects of reaction temperature, BR concentration, the ratio of Zn^{2+} to H_3BTB ligand and the input concentration of Zn^{2+} to H_3BTB on particle size and berberine loading rate were explored in turn. Finally, it was concluded that the reaction temperature was 80°C, the BR concentration in the system was 1.5 mg/mL, the ratio of Zn^{2+} to H_3BTB was 3, the input concentration of H_3BTB was 3 mg/mL, and the reaction time was 3 days, which were the best reaction conditions.

Preparation of BR-loaded Zn-BTB (BR@Zn-BTB)

BR@Zn-BTB nanoparticles were prepared by a facile one-pot synthetic method. Typically, the aqueous solution of berberine (3 mL, 3 mg/mL) was added into the clear DMF solution (3 mL) containing H_3BTB (18 mg, 0.041 mmol) and $ZnCl_2$ (6.82 mg, 0.123 mmol) and the mixture was stirred at 80°C for 3 days. The precipitated yellow product was obtained by centrifugation at 10000 rpm for 5 min, washed with methanol three times and dried under vacuum overnight at 70°C.

Fabrication of the hydrogels incorporating BR@Zn-BTB

The aqueous solutions of ROS-responsive linker TPA and PVA with an initial concentration of 50 mg/mL for both were prepared according to the previous repor.[37] Pure hydrogel could be obtained by mixing the above prepared PVA and TPA with equal volumes. Due to the viscosity of hydrogel, it is difficult to obtain homogeneous composites by mixing the hydrogel and Zn-BTB or BR@ZnBTB particles. Thus, the homogeneous composites of Zn-BTB/Gel (denoted as B-Gel) or BZ-Gel (denoted as Z-Gel) were freshly prepared as required for each experiment according to the following process. The BR@ZnBTB particles (10 mg) were added to the PVA solution (10 mL, 50 mg/mL) under stirring for 6 h to give the concentration of 1 mg/mL for BR@ZnBTB in PVA. Then, the solution of TPA (40 μL, 50 mg/mL) was added into the solution of the prepared PVA (40 μL, 50 mg/mL) which contained BR@Zn-BTB (1 mg/mL) and stirred for 2 min to give homogeneous hydrogel encapsulated BR@Zn-BTB composites of BZ-Gel (40 μL, 1 mg/mL). Here, the volume of 40 μL and the concentration of 1 mg/mL for BZ-Gel represents its initial reaction volume and concentration. B-Gel and Z-Gel were prepared as the same procedure as BZ-Gel.

The BR and Zn^{2+} released from the BR@Zn-BTB nanoparticles and BZ-Gel scaffold *in vitro*

The dialysis bag was used to explore the release behavior of BR and Zn^{2+} *in vitro*. Four groups of BR@Zn-BTB (3.97 mg, 4.78 mg, 4.98 mg, and 5.53 mg) was respectively dissolved in PBS (1 mL), which were then placed in the activated dialysis bag. The four dialysis bags were immersed into 20 mL phosphate-buffered solution (PBS, pH 6.5, 7.0, 7.4, and 8.0) at 37°C in a shaker with a speed of 100 r/min. At each defined time point, 2 mL of the release medium was collected for the detection and replaced with an equal volume of fresh PBS.

BZ-Gel (3 mL, 1 mg/mL) were placed in an activated dialysis bag and then placed in 20 mL PBS (pH 7.4) at 37°C in a shaker with a speed of 100 r/min to study the sustained release of BR and Zn^{2+}. At each defined time point, 2 mL of the released medium was collected for the detection and replaced with an equal volume of fresh PBS.

Hydrogel degradation behavior for ROS scavenging *in vitro*

The pure hydrogel (1 mL) was added to 10 mL PBS with or without H_2O_2 (100 mM) at room temperature. The two samples were photographed to monitor the changes of the hydrogel at 0, 1, 1.5, and 2 h.

As the same process mentioned above, the pure hydrogel (1 mL) was added to 10 mL PBS with H_2O_2 (100 mM), then 0.5 mL solution was taken out at 0, 1, 1.5, and 2 h. Each solution was further incubated with horseradish peroxidase (HRP, 50 μL, 5 μg/mL) and tetramethylbenzidine (TMB) (100 μL, 10 mg/mL) for 5 min at 37°C in dark. UV-Vis was used to detect the characteristic absorption peaks at 650 nm at 0, 1, 1.5, and 2 h.

Antibacterial test

The inhibition zone method was used to test the antibacterial ability of the different nanoparticles. Three types of bacteria of *Escherichia coli*, *Staphylococcus epidermidis* and *Staphylococcus aureus* were activated twice, and the concentration for each of them was then adjusted to 5×10^7 CFU/mL. 200 μL of bacterial suspension was cultured on Luria-Bertani (LB) medium and the Gel (100 μL), B-Gel (100 μL, 1 mg/mL), Z-Gel (100 μL, 1 mg/mL), and BZ-Gel (100 μL, 1 mg/mL) were introduced. Then LB medium was placed on the bacteria incubator for 24 h. The antibacterial activity was investigated by measuring the zone of inhibition (clear zone).

Cytotoxicity assay

To screen for the appropriate dosing concentration, the HaCaT cells and HSF cells (1×10^4 cells/well, 96-well plate) were incubated with different concentrations of BR, H_3BTB, Zn-BTB, and BR@Zn-BTB for 24 h under 5% CO_2 at 37°C to obtain the appropriate dosing concentration. Then the cell viability was measured by CCK-8 assay (Bio-sharp, China).

After screening the appropriate dose concentration, the HaCaT and HSF cells were used to evaluate the cytotoxicity of Zn-BTB and BR@Zn-BTB. HaCaT and HSF cells (1×10^4 cells/well) were seeded in 96-well plates and incubated with Zn-BTB (40 μg/mL) and BR@Zn-BTB (40 μg/mL) particles for 1, 2 and 3 days, respectively. The cells viability was then evaluated by CCK-8. The absorbance value of samples was measured at 450 nm using an enzyme-linked immunosorbent assay (ELISA) plate reader (Molecular Devices).

After verifying that 40 μg/mL is a safe concentration, hydrogel loading and live/dead staining were used to further evaluate the biocompatibility of the composite system (BZ-Gel). HaCaT and HSF cells (5×10^4 cells/well) were seeded in 24-well plates and incubated with PBS (40 μL), Gel (40 μL), Z-Gel (40 μL, 1 mg/mL) and BZ-Gel (40 μL, 1 mg/mL) for 1, 2 and 3 days, respectively. The cell viability was measured through a live/dead kit (Green fluorescence: Calcein-AM indicates live cells, Red fluorescence: Propidium Iodide (PI) indicates dead cells) based on the manufacturer's protocol and observed by fluorescence microscope (IX53, Olympus, Japan).

Cell migration assay

The effect of BZ-Gel on the migration of HaCaT and HSF cells was evaluated *in vitro* using wound healing migration experiments. Specifically, HaCaT (5×10^5 cells/well) and HSF (5×10^5 cells/well) were seeded in 24-well plates. After 24 h incubation, the cell scratch was created with a sterile pipette tip, washed with PBS, and co-cultured with PBS (40 μL), Gel (40 μL), Z-Gel (40 μL, 1 mg/mL), and BZ-Gel (40 μL, 1 mg/mL) respectively in high glucose cell culture medium (13.5 g/L) for 48 h. The cells were photographed with a microscope.

Intracellular ROS scavenging evaluation

HSF (5×10^4 cells/well) was seeded in a 24-well plate and incubated with the following additives after 12 h: 1) 10 μL H_2O_2 (final concentration 100 μM); 2) 10 μL H_2O_2 and 40 μL Gel; 3) 10 μL H_2O_2 and Z-Gel (40 μL, 1 mg/mL); 4) 10 μL H_2O_2 and BZ-Gel (40 μL, 1 mg/mL). After 24 h of incubation, the cells were incubated with DCFH-DA for 20 min. Then, after washing three times with PBS, DCF fluorescence (λ_{ex} = 488 nm, λ_{em} = 525 nm) was measured using a fluorescence microscope (IX53, Olympus, Japan).

Quantitativereal-time polymerase chain reaction (qRT-PCR)

To verify the effect of BZ-Gel on the expression of MMP9 and TIMP1 under a high glucose environment (13.5 g/L),[45] HaCaT (1 × 10^6 cells/well) were seeded in a 6-well plate and cultured with BZ-Gel (40 μL, 1 mg/mL), Gel (40 μL) and Z-Gel (40 μL,1 mg/mL), and PBS as the control (40 μL) for 48 h.

To evaluate the anti-inflammatory effect of BZ-Gel, RAW264.7 cells (1 × 10^6 cells/well) were seeded in a 6-well plate. After stimulated with LPS (0.5 μg/mL) for 24 h, RAW264.7 cells cultured with Gel (40 μL), Z-Gel (40 μL, 1 mg/mL), BZ-Gel (40 μL, 1 mg/mL) and PBS (40 μL) as the control for 48 h. Then detected the expression of IL-6, IL-1bβ and TNF-α.

The total RNA was obtained and extracted by using Trizol (Invitrogen, Waltham, MA, USA). cDNA was synthesized from total RNA (1 μg) using 5× all-in-one RT Mastermix (ABM, Germany) at 37°C for 10 min, 65°C for 15 min, and at 95°C for 3 min. qRT-PCR was conducted using TB Green® Premix Ex Taq™ II (Takara, Japan). The sequence of MMP9 and TIMP1 used for qRT-PCR reactions were shown in Table S1. The sequence of IL-6, IL-1bβ and TNF-α used for qRT-PCR reactions were shown in Table S2. All primers were found in the Primer Bank and synthesized by Genewiz (Shanghai), the specificity of the primers was confirmed before being used.

Wound healing assessment

The experimental animals in this study were purchased from the Guangdong Provincial Animal Center, and the animal experiments were approved by the Guangdong Provincial Animal Ethics Committee. The diabetic mice were induced by streptozotocin (STZ) according to previous reports previous reports.[55] Briefly, to induce diabetic Mellitus-like symptoms, 6–8 weeks C57BL/6 mice were injected intraperitoneally with STZ (50 mg/kg body weight per day) until the blood glucose levels were continuously higher than 300 mg/dL (16.7 mM). The blood glucose levels were measured by using glucose meters (Accu-Chek Performa). The induced diabetic mice were randomized into the control, Gel, Z-Gel, and BZ-Gel groups according to their blood glucose levels and anesthetized with tribromoethanol (1.25%). After the mice were anesthetized, a standardized full-thickness wound with a diameter of 10 mm on the dorsum of each mouse was created. After 3 hours of exposure to UV light, the Gel (150 μL), Z-Gel (150 μL, 1 mg/mL), and BZ-Gel (150 μL, 1 mg/mL) were applied to the wound beds and covered with gauze. The images of the wounds were photographed on days 0, 5, 9, 12 and the size of the wound was measured. The formula for calculating the size of diabetic wounds is as follows:

$$\text{The percentage of wound size reduction (\%)} = (Day_0 - Day_x)/Day_0 \times 100\%:$$

where the initial area of the wound is marked as Day_0 and Day_x is the area of the wound on day x ($x \geq 1$) is marked as dayx. The mice were sacrificed at day 9 and day 12 after surgery.

Histological staining of wound tissue in diabetic mice

To characterize the skin re-epithelialization of diabetic mice, histological staining of wound tissue sections was used. After the mice were sacrificed on Day_9 and Day_{12}, 4% paraformaldehyde was used to fix the skin tissues in the wound bed for 24 h. Then, paraffin-embedded tissues were sectioned into 4 μm thickness slices, and hematoxylin and eosin (H&E) staining and Masson's trichrome staining were performed.

Image J counts inflammatory cells

Open the picture you want to edit.

Grayscale transformation: Select Image->Type->8-bit in the menu bar to convert the image to be processed into an 8-bit grayscale image;

Grayscale threshold setting: Select Image->Adjust->Threshold in the menu bar; according to the grayscale value configuration of the picture, extract the threshold value of the maximum and minimum grayscale values in the picture, drag the grayscale selection bar, and select the appropriate grayscale value range;

Manual denoising: First, select a drawing tool according to the shape of the part to be processed in the picture, taking an arbitrary curve as an example; use the cropping tool to crop the part that needs to be processed in the picture;

Scale bar setting: To use this graph as a picture for cell counting, you need to first perform a scale bar setting. The settings are arranged as follows; select the line drawing tool to draw a straight line on the graph;

Counting: After setting the scale, you can count the cells. Select Analyze->Analyze Particles.

Image J quantify Masson staining

Step 1: In ImageJ software, choose File -> Open to open a Masson staining image to be analyzed.

Step 2: Select image→type→RGB stack.

Step 3: Select image→adjust→threshold.

Step 4: Adjust the threshold so that collagen is selected (red means selected).

Step 5: Select analyze→measure.

Step 6: Area represents the pixels occupied by the red area, and %Area represents the proportion of the red area in the entire image.

qRT-PCR of the wound tissue

The total RNA of re-epithelized skin tissue was extracted by Trizol (Invitrogen, Waltham, MA, USA). The isolated RNA (1 μg) was then reversely transcribed into cDNA using 5 × all-in-one RT Mastermix (ABM, Germany) at 37°C for 10 min, 65°C for 15 min, and at 95°C for 3 min. qRT-PCR was conducted using TB Green® Premix Ex Taq™ II (Takara, Japan). GAPDH was used as the reference gene and the primer sequences detected in this study were shown in Table S2.

QUANTIFICATION AND STATISTICAL ANALYSIS

Randomization was used to assign the various samples to the experimental groups and treatment conditions for all *in vivo* studies. All quantitative results were expressed as mean G Standard Error of Mean (SEM). The data was analyzed using Unpaired Student's *t* test or one-or two-way ANOVA on GraphPad Prism 8.0. A value of $p < 0.05$ was considered to be statistically significant.